CHALMERS
UNIVERSITY OF TECHNOLOGY

Design and Evaluation of Antenna System for Non-Invasive Detection of Intracranial Hemorrhaging

Master's thesis in Biomedical Engineering

Xuerui Mi

Supervisor: Andreas Fhager

Department Of Biomedical Engineering
CHALMERS UNIVERSITY OF TECHNOLOGY
Gothenburg, Sweden 2026

Master's thesis 2026

Design and Evaluation of Antenna System for Non-Invasive Detection of Intracranial Hemorrhaging

Xuerui Mi

CHALMERS
UNIVERSITY OF TECHNOLOGY

Department Of Electrical Engineering
Division of Biomedical Engineering
Chalmers University of Technology
Gothenburg, Sweden 2026

Design and Evaluation of Antenna System for Non-Invasive Detection of Intracranial Hemorrhaging

Supervisor: Andreas Fhager,Department Of Electrical Engineering
Examiner: Andreas Fhager, Department Of Electrical Engineering

Master's Thesis 2026
Department Of Electrical Engineering

Chalmers University of Technology
SE-412 96 Gothenburg
Telephone +46 767478512

Typeset in LaTeX

Gothenburg, Sweden 2026

Abstract

Intracerebral hemorrhage (ICH) is a life-threatening form of stroke, responsible for approximately 3.3 million deaths annually worldwide and contributing to a global economic burden exceeding $890 billion per year. Clinical evidence shows that early detection and rapid intervention significantly reduce mortality, underscoring the need for fast and reliable diagnostic techniques.

In this study, we propose a low-cost, portable microwave-based system for early detection of intracerebral hemorrhage. The system integrates a wearable circumferential antenna array for signal transmission and reception with an image reconstruction algorithm for recovering internal brain structures, enabling rapid and non-invasive detection of hemorrhagic regions.

A major challenge in such systems is that microwave signals radiated by the antennas propagate in multiple directions, causing neighboring antennas to receive not only signals transmitted through brain tissues but also unwanted components traveling outside the region of interest. These undesired signals do not contain useful intracranial information and can degrade imaging accuracy. To mitigate this issue, dielectric gel is applied to the lateral and posterior sides of the antennas to suppress these unwanted signal components.

To achieve this, we focus on the dielectric properties of the gel, specifically its relative permittivity and conductivity. Through controlled comparative evaluations, the effects of permittivity and conductivity are systematically investigated, and optimal values are identified at approximately 40 and above 5 S/m, respectively. Based on these target properties, a material is synthesized using silicone rubber as the base matrix and carbon black (CB) as a conductive filler. The fabricated material exhibits a relative permittivity of approximately 15 and a conductivity around 15 S/m, approaching the target values while remaining practically realizable. The proposed material is incorporated into the antenna configuration within a simplified head model in electromagnetic simulations. The antennas placed along the lateral and posterior sides are loaded with the synthesized material, and the resulting S-parameters are collected for image reconstruction using the Delay-Multiply-and-Sum (DMAS) algorithm. The reconstructed images demonstrate improved localization of hemorrhage regions compared to the case without gel, showing clearer and more focused imaging results.

Keywords—Microwave imaging, Brain hemorrhage, Multipath wave, Dielectric properties, S-parameters, Gel.

Acknowledgements

I would like to express my deepest gratitude to the many individuals who have supported me throughout this journey.
First and foremost, I would like to thank my supervisor, Andreas Fhager. Words cannot fully express how grateful I am for his mentorship. He has been incredibly patient in answering my questions and consistently methodical in guiding the project. Beyond his technical guidance, his professionalism and steady support gave me reassurance whenever I felt anxious. I truly could not have asked for a better supervisor. I would also like to express my sincere gratitude to Rikard Karlsson for his guidance and support throughout this work. I am very grateful to August Ekman for generously sharing his knowledge and expertise. I would further like to thank Yang Jian for his valuable advice and insights on the antenna design. My sincere thanks also go to Mattia de Lazzari for his kindness and for always being willing to help and answer my questions.
Finally, I would like to extend my special thanks to Xuezhi Zeng, the Director of Biomedical Engineering. Her guidance on topic selection, project planning, and progress management was invaluable to the successful completion of my thesis.

Xuerui, Gothenburg, 2026

List of Acronyms

Below is the list of acronyms that have been used throughout this thesis listed in alphabetical order:

DMAS	Delay Multiply and Sum
UWB	Ultra Wide Band
VNA	Vector Network Analyzer

Contents

List of Figures

1 Introduction

Stroke is a major global health issue, causing approximately 6.5 million deaths annually and remaining a leading cause of long-term disability worldwide [1, 2]. Rapid diagnosis and timely treatment are critical, as delays can significantly reduce the effectiveness of time-sensitive interventions and worsen clinical outcomes.

Current stroke assessment relies on clinical evaluation and brain imaging, with non-contrast CT used to exclude intracranial hemorrhage and MRI providing higher sensitivity for detecting acute ischemia [5]. However, access to imaging facilities and clinical workflow constraints often introduce delays in diagnosis, particularly in pre-hospital settings. These limitations motivate the development of rapid and accessible diagnostic approaches for earlier stroke detection.

Microwave imaging (MWI) has emerged as a promising modality for stroke detection by exploiting dielectric-property contrast between healthy brain tissue, blood, and ischemic regions [7, 13]. Its potential for fast, non-ionizing, and portable operation makes it particularly suitable for pre-hospital triage [14].

However, despite these advantages, several practical challenges hinder its clinical translation, particularly in scenarios requiring rapid and low-maintenance operation. Many existing systems rely on liquid coupling media to facilitate signal propagation and suppress multipath interference [15, 16]. However, such media may exhibit changes in physical properties over time, compromising electromagnetic stability and limiting durability in repeated use.

These limitations motivate the exploration of alternative lossy materials that can provide effective multipath suppression while offering improved robustness, stability, and ease of handling. In this work, we explore the use of a durable and stable coupling material for microwave-based brain imaging, aiming to suppress multipath interference.

1.1 Stroke Background

Stroke is a time-critical neurological emergency that requires rapid diagnosis and intervention. It is defined as an acute neurological deficit of vascular origin and can lead to irreversible brain injury within minutes if untreated, often presenting with symptoms such as focal weakness, visual impairment, or speech disturbance [8]. Clinically, stroke is broadly classified into two major types: ischemic stroke, caused by arterial occlusion, and hemorrhagic stroke, caused by intracranial bleeding. Among these, ischemic stroke accounts for the majority of cases, while hemorrhagic stroke, although less common, is associated with more severe early neurolog-

ical deterioration and higher early mortality [8, 9].
Hemorrhagic stroke, particularly intracerebral hemorrhage, is characterized by bleeding within brain tissue that leads to rapid neurological decline. Extravasated blood can directly damage surrounding brain structures and increase intracranial pressure, contributing to high case fatality and severe clinical outcomes [8, 9]. Due to its rapid progression and high mortality risk, accurate and timely detection of intracranial hemorrhage is essential in both pre-hospital and in-hospital settings.
Stroke outcomes vary widely depending on lesion size, location, and the timeliness of medical intervention. Clinical severity can range from transient ischemic attacks with fully reversible symptoms to large infarctions or hemorrhages causing permanent disability or death [8]. Case fatality is influenced by multiple factors, including delays in symptom recognition, severity of the vascular event, and involvement of critical brain regions such as the brainstem [9]. Although timely treatment—such as reperfusion therapy for ischemic stroke and surgical or medical management for hemorrhagic stroke—can improve outcomes, a substantial proportion of patients still experience long-term functional impairment [8, 9]. These challenges highlight the critical importance of rapid and reliable diagnostic approaches for early stroke detection.

1.2 Microwave Imaging

Microwave imaging (MWI) is a non-ionizing imaging modality with strong potential for rapid and portable brain diagnostics. It operates using electromagnetic waves in the microwave frequency band, typically in the sub- to low-gigahertz range, where wavelengths are sufficiently long to penetrate the head while still maintaining useful spatial resolution [10, 11], although some studies extend to higher frequencies up to around 10 GHz. Compared with conventional imaging techniques such as X-ray computed tomography (CT) and magnetic resonance imaging (MRI), MWI offers several advantages, including low-cost hardware implementation, compact system design, and fast data acquisition. These features make it particularly attractive for pre-hospital triage and bedside monitoring in time-critical conditions such as stroke and intracranial hemorrhage [7, 13, 14].
The fundamental imaging mechanism of MWI relies on dielectric-property contrast between different biological tissues. The electromagnetic response of biological tissue at microwave frequencies is commonly described by the complex relative permittivity $\varepsilon_r^*(\omega)$,

$$\varepsilon_r^*(\omega) = \varepsilon_r'(\omega) - j\frac{\sigma(\omega)}{\omega\varepsilon_0}, \tag{1.1}$$

where $\varepsilon_r'(\omega)$ is the relative permittivity, $\sigma(\omega)$ is the effective conductivity, ω is the angular frequency, ε_0 is the permittivity of free space, and j is the imaginary unit [69]. Different tissues exhibit distinct dielectric properties; for example, water-rich tissues and blood typically have higher permittivity and conductivity than bone or fat, and pathological changes can further modify these properties [69]. This contrast enables MWI to distinguish between normal and abnormal regions, such as hemorrhagic lesions.

A typical MWI system for brain imaging consists of a multistatic antenna array and an image reconstruction process. Multiple wideband antennas are arranged around the head, where each antenna sequentially transmits microwave signals while the others measure the scattered fields. This procedure is repeated across different transmit–receive combinations to collect scattering data associated with the internal dielectric distribution [7, 10]. The acquired data are then processed through an inverse problem, commonly formulated as electromagnetic inverse scattering or tomographic reconstruction, to recover images of the spatial variations in permittivity and conductivity. Such approaches have been applied to detect intracranial abnormalities, including hemorrhagic stroke, by exploiting the higher dielectric properties of blood relative to surrounding brain tissue [13].

1.3 Coupling Media

In microwave imaging, the coupling medium between the antenna array and the body plays a key role in improving power transfer, reducing surface-wave–dominated multipath components, and enhancing the robustness of image reconstruction. Although air-coupled systems provide greater operational convenience and enable non-contact bedside measurements, they suffer from a strong impedance mismatch between air ($\epsilon_r \approx 1$) and high-permittivity biological tissues. This mismatch leads to substantial reflection at the skin interface, thereby reducing the electromagnetic energy coupled into deeper regions and increasing multipath interference[56]. For this reason, physical coupling media are commonly introduced to improve impedance matching and to attenuate surface-wave propagation.

From the perspective of mechanical form factor and maintenance requirements, coupling materials can be broadly grouped into three classes: liquid gels, semi-solid gels, and solid layers. This section reviews representative work in each category and summarizes the design constraints for durable, solid-state matching layers.

The key challenge in designing coupling media lies in achieving appropriate dielectric properties. In particular, permittivity and conductivity must be carefully selected, as they influence different aspects of electromagnetic wave propagation. Materials that deviate from suitable ranges may either reflect excessive energy at interfaces or fail to sufficiently attenuate unwanted scattered signals.

This behavior can be understood through the relative contributions of conduction and displacement currents in time-harmonic electromagnetic fields. The total current density is given by

$$\mathbf{J}_{\text{tot}} = \sigma \mathbf{E} + j\omega\varepsilon\mathbf{E}, \tag{1.2}$$

where σ represents electrical conductivity, ω is the angular frequency, and ε is the permittivity. The ratio between these terms determines the effective loss characteristics of the material and directly influences wave attenuation and propagation.

A sufficiently high conductivity is beneficial for reducing multipath interference by increasing electromagnetic losses. Such losses help attenuate reflected and scattered fields within the imaging domain. However, excessive conductivity may also reduce penetration depth, requiring careful optimization.

At the same time, permittivity plays a key role in impedance matching at material

interfaces. When the dielectric properties of two media are similar, reflections at the interface are reduced, improving power transmission into biological tissue [39].
To address these requirements, this work focuses on silicone-based composite materials loaded with conductive fillers such as carbon black. Carbon-black-loaded polymers are widely used for tuning dielectric properties at microwave frequencies, enabling controlled adjustment of conductivity and permittivity through filler concentration and dispersion [88, 40].

1.3.1 Liquid Media

Liquid baths are a common solution in microwave tomography. By immersing the anatomical target in a tank filled with water, saline, or glycerin mixtures, a high-permittivity, moderately lossy background is created. This environment improves impedance matching and attenuates surface-wave propagation. Meaney *et al.* characterized glycerin–water mixtures across 0.1–25 GHz and reported that mixtures with 70–90% glycerin exhibit conductivities above 1 S/m in the 1–3 GHz band [20]. This work showed that the liquid composition can be tuned to balance coupling efficiency with multipath attenuation.
More recently, Fang *et al.* introduced a shelf-stable, food-grade emulsion designed specifically for microwave imaging [16]. Unlike glycerin mixtures, this protein-stabilized emulsion is bubble-free and maintains stable dielectric properties over several days, with low thermal sensitivity. While these liquid solutions offer strong tunability, they require fluid handling, tank maintenance, and periodic replacement, which poses integration challenges for compact or clinical bedside systems. In addition, the interface between the patient and the liquid presents practical challenges, particularly in pre-hospital settings, where immersing a patient in a liquid medium is not feasible.

1.3.2 Semi-solid Media

Semi-solid gels provide an intermediate solution by enabling localized coupling without bulky immersion setups. Guerrero Orozco *et al.* developed a lossy saline–agar gel placed directly behind the antenna to create a localized coupling environment [50]. This approach approximates the effect of a global bath, while their results showed that increasing gel losses reduced multipath interference and improved image repeatability.
The theoretical basis of matching media was analyzed by Lui and Andreas Fhager, who investigated how the permittivity and conductivity of the medium affect electromagnetic wave propagation, including reflection, transmission, and absorption within biological tissues [21, 22]. These studies primarily consider matching media placed between air and tissue to reduce impedance mismatch and improve wave penetration.
Similarly, Koutsoupidou *et al.* [43] investigated a dielectric matching cap surrounding the head to enhance electromagnetic coupling at the air–tissue interface, demonstrating reduced reflections and improved penetration and sensitivity.
Although the lossy gel used in this work serves a different purpose—namely sup-

pressing antenna coupling and multipath effects rather than achieving impedance matching—the insights from these studies regarding the role of permittivity and conductivity provide useful guidance. In this sense, the design of the lossy gel can be informed by similar electromagnetic principles, even though the intended function differs.

These studies collectively suggest that while semi-solid materials offer electromagnetic advantages, their mechanical compliance may still present practical challenges compared to fully solid implementations.

1.3.3 Solid Media

For microwave imaging systems intended for repeated clinical use, solid coupling layers provide a more stable and maintenance-free alternative to conventional liquid media. By replacing liquid-filled tanks with a reusable solid layer integrated directly into the antenna array, the system achieves a stable electromagnetic environment while also offering improved mechanical protection for the antennas. In addition, solid layers eliminate issues such as leakage, evaporation, and frequent refilling, which are inherent to liquid-based systems and increase operational complexity.

Despite these advantages, replacing liquid coupling media with solid materials introduces stringent requirements on material properties. The solid layer must replicate the favorable electromagnetic characteristics of liquid or semi-solid matching media while maintaining sufficient mechanical robustness. Such matching media are known to improve impedance matching at the air–skin interface and enhance the transmission of electromagnetic energy into biological tissues [38, 39].

1.4 Antennas for Microwave Imaging

Antennas play a central role in microwave imaging systems, serving as both transmitters and receivers of electromagnetic waves interacting with biological tissues. A wide variety of antenna designs has been proposed, each offering different trade-offs in terms of bandwidth, directivity, compactness, and compatibility with lossy and inhomogeneous media. Common examples include bow-tie antennas, Vivaldi antennas, and monopole-based structures, which can be used either as individual elements or in antenna arrays for imaging.

Bow-tie and Vivaldi antennas have been widely investigated due to their ultra-wideband characteristics and directional radiation properties. For instance, self-grounded bow-tie antennas provide stable radiation patterns and good impulse-response behavior [44], while also maintaining wide bandwidth under dielectric loading conditions, such as in immersion-based imaging setups [45]. Similarly, Vivaldi antennas offer high directivity and efficient energy coupling into biological tissue, with variations such as fern-shaped designs improving near-field focusing capabilities [46] and compact antipodal configurations being explored for brain imaging applications [47]. While these antenna types are well suited for certain scenarios, particularly where high directivity is required, they are generally less compatible with compact, wearable, or strongly body-coupled imaging systems.

Monopole antennas are particularly well suited for wearable microwave imaging systems due to their simplicity, robustness, and compatibility with lossy coupling environments. The following discussion highlights their key advantages from the perspectives of practical implementation, electromagnetic performance, and system-level modeling.

From a practical implementation perspective, monopole antennas offer compact geometries and ease of integration. Compared with more complex antenna structures, monopoles can be readily incorporated into wearable and body-conformal platforms, such as helmet-based or gel-coupled imaging systems. Their simple design also facilitates fabrication and alignment in multi-element measurement setups.

From an electromagnetic performance standpoint, monopole antennas exhibit radiation characteristics that are well suited for microwave imaging. They have been extensively studied in the low-GHz frequency range, where signal penetration into biological tissues is significantly improved. For example, Thakkar *et al.* [48] developed compact monopole structures operating between 0.6 and 1.5 GHz, demonstrating stable radiation behavior and suitability for multi-element wearable arrays. Their omnidirectional radiation patterns are particularly advantageous for imaging systems that rely on distributed sensing around a target region.

In addition, the relatively simple electromagnetic behavior of monopole antennas facilitates accurate numerical modeling in inverse scattering algorithms. This advantage is demonstrated in the work of Meaney *et al.* [55], where a 16-element circular monopole array was used in a clinical prototype for breast cancer detection. Their study showed that, when operated in a lossy coupling medium such as water or saline, monopoles can achieve broadband performance while maintaining stable impedance matching. These experiments also provided important insights into in vivo tissue properties, with reported relative permittivity values (ε_r) ranging from approximately 20 to 36.

Despite these advantages, the performance of monopole antennas remains strongly dependent on the surrounding dielectric environment. In particular, their impedance matching, radiation efficiency, and multipath response are significantly influenced by the properties of the coupling medium. Guerrero Orozco *et al.* [50] demonstrated that integrating lossy semi-solid gels with monopole sensors can effectively suppress multipath reflections and improve measurement repeatability, highlighting the critical role of controlled dielectric environments.

Motivated by these considerations, monopole antennas are adopted in this work as the primary sensing elements for a gel-based microwave imaging system. Their compact geometry, ease of integration, and robustness in lossy media make them well aligned with the requirements of solid coupling layers, which are investigated in the following sections.

1.5 Image Algorithms

In the early development of medical microwave imaging, substantial research focused on quantitative microwave tomography (MWT). Early work employed iterative inverse-scattering algorithms to reconstruct the spatial distribution of tissue dielectric properties, such as permittivity and conductivity [60, 61]. However, the associated nonlinear and ill-posed inverse problem governed by Maxwell's equations is computationally intensive and often requires long execution times, which limits the practicality of quantitative tomography for time-critical diagnosis and continuous monitoring [58].

To mitigate these limitations, ultra-wideband (UWB) radar-based qualitative imaging methods, notably confocal microwave imaging, were proposed as computationally efficient alternatives [62, 63]. This approach transmits short UWB pulses into the tissue and records backscattered signals from dielectric discontinuities. By applying appropriate time delays to align signals corresponding to a given focal point, scattering contributions from that location can be coherently combined [58].

The standard Delay-and-Sum (DAS) beamformer subsequently became a baseline method for this modality due to its simplicity and consistent performance. In DAS, the received signals are time-shifted according to the expected propagation delay from each antenna to a focal point, and then summed to enhance coherent reflections while suppressing incoherent noise. Nevertheless, DAS is susceptible to strong clutter, particularly dominant reflections from the air–skin interface, which reduce image contrast and can obscure smaller targets [59].

To suppress clutter and improve the dynamic range of DAS-based imaging, several more advanced algorithms were developed, including the Microwave Imaging via Space-Time (MIST) beamforming scheme introduced by Bond *et al.* [85]. While MIST employs multi-channel space–time equalizers to compensate for dispersion and suppress clutter, Lim *et al.* [59] noted that it depends on accurate prior information about the propagation medium and requires complex filter-bank design. The authors also observed that other adaptive techniques, such as the Generalized Likelihood Ratio Test (GLRT) and Time Reversal (TR), can be sensitive to non-uniform background noise.

To achieve clutter suppression with reduced algorithmic complexity, the Delay-Multiply-and-Sum (DMAS) beamformer was introduced [59]. Similar to DAS, the received signals are first time-aligned according to the assumed propagation delay. However, instead of directly summing the aligned signals, DMAS performs a pairwise multiplication between signals from different antenna channels before summation. This nonlinear operation effectively emphasizes coherent signal components associated with true scatterers, as in-phase signals produce consistently positive contributions, while incoherent noise and clutter tend to cancel out due to random phase differences. As a result, DMAS can attenuate out-of-phase multipath contributions and improve the signal-to-clutter ratio (SCR), leading to sharper target localization compared with standard DAS.

Beyond nonlinear beamforming strategies such as DMAS, recent studies have explored weighting schemes that exploit measurement geometry. In particular, the Weighted Delay-and-Sum (WDAS) beamformer[86] extends the conventional DAS formulation by introducing channel-dependent weighting factors into the summation process. After time alignment, each signal contribution is scaled according to a predefined weight, which reflects its expected reliability.

These weights are typically determined based on the transmitter–receiver distance (TRD), under the assumption that channels with shorter propagation paths experience less attenuation and dispersion, and therefore retain stronger coherent com-

ponents . Signals acquired from antenna pairs with shorter separations may exhibit higher coherence and contain more reliable target information, whereas distant pairs can be more susceptible to decorrelation and noise.
Overall, these developments highlight the progression from linear beamforming methods such as DAS to more advanced approaches that incorporate signal coherence and geometric weighting. In this work, DMAS-based processing is adopted as the primary imaging strategy due to its ability to enhance coherent scattering while suppressing clutter, and it is further examined in combination with geometry-based weighting to improve reconstruction performance.

1.6 Purpose and Aim

Recent progress in microwave imaging has been driven by improvements in coupling media, antenna design, measurement technology, and imaging algorithms. In particular, the transition from liquid-based media to semi-solid gels, together with the development of wideband antenna architectures, has significantly enhanced system performance and measurement flexibility.
Despite these advances, the practical deployment of microwave imaging systems in clinical settings remains challenging. Key issues include sensitivity to dielectric loading, which affects antenna performance, multipath propagation that degrades image quality, and variability at the antenna–tissue interface caused by inconsistent contact conditions.
These limitations highlight the need for a systematic investigation of the interaction between antennas and coupling media. In particular, understanding how the electromagnetic properties of the coupling layer and the antenna configuration jointly influence impedance matching, wave propagation, and imaging performance is critical for improving system reliability and robustness.

1.6.1 Research Aim

The aim of this work is to investigate and optimize a gel-assisted microwave imaging configuration for brain applications, with a particular focus on improving electromagnetic coupling and suppressing multipath effects in the frequency range of 0.5–1.5 GHz.

1.6.2 Contributions

The main contributions of this work can be summarized as follows:

1. **Impact of Coupling Parameters:** A systematic investigation of how the permittivity (ε_r) and conductivity (σ) of the coupling medium affect wave propagation. A practical design region is identified, targeting $\varepsilon_r \approx 40$ and $\sigma \gtrsim 5$ S/m at 1 GHz for head imaging applications.
2. **Gel Material Synthesis:** A practical approach for realizing coupling media with suitable dielectric properties is proposed using a silicone-based matrix combined with carbon black as a conductive filler. This approach enables tunable conductivity while maintaining mechanical stability, providing a feasible

compromise between target dielectric performance and material fabrication constraints.

3. **Imaging Validation Using DMAS:** The effectiveness of the optimized coupling conditions is evaluated through full-wave simulations and S-parameter-based reconstruction using the DMAS beamforming algorithm. This step demonstrates how improved coupling and reduced multipath propagation translate into enhanced target localization in microwave imaging.

1.6.3 Limitations

Some limitations of this study should be noted. First, the evaluation is based on simplified numerical head models rather than anatomically realistic or experimental setups, which may not fully capture in vivo tissue heterogeneity. Second, the study focuses on simulation-based validation using a single reconstruction algorithm (DMAS), and does not include experimental measurements.

1.6.4 Acknowledgment

The author would like to acknowledge the use of AI-assisted tools for language refinement and clarity improvement. All scientific content, methodology, and interpretations were developed independently by the author.

2
Theory

This chapter introduces the electromagnetic and antenna theory required to understand the design, simulation, and analysis of microwave antennas used in near-field biomedical imaging. The concepts covered include electromagnetic wave propagation, antenna impedance behavior, scattering parameters, transmission line fundamentals, and the computational principles of CST Studio Suite. Together, these topics provide the theoretical foundation for interpreting how gel permittivity, conductivity, and antenna–tissue interactions affect the antenna performance investigated in this thesis.

2.1 Electromagnetic Fundamentals

2.1.1 Maxwell's Equations

Electromagnetic phenomena are governed by Maxwell's equations, which describe the generation and evolution of electric and magnetic fields in space and time [72, 71]. In differential form, they are expressed as:

$$\nabla \cdot \mathbf{D} = \rho, \tag{2.1}$$

$$\nabla \cdot \mathbf{B} = 0, \tag{2.2}$$

$$\nabla \times \mathbf{E} = -\frac{\partial \mathbf{B}}{\partial t}, \tag{2.3}$$

$$\nabla \times \mathbf{H} = \mathbf{J} + \frac{\partial \mathbf{D}}{\partial t}. \tag{2.4}$$

Here, $\mathbf{E}$ denotes the electric field intensity (V/m), $\mathbf{H}$ the magnetic field intensity (A/m), $\mathbf{D}$ the electric flux density (C/m^2), and $\mathbf{B}$ the magnetic flux density (T). The quantities ρ and $\mathbf{J}$ represent the free charge density (C/m^3) and current density (A/m^2), respectively.
To relate the field quantities, constitutive relations are introduced. For linear, isotropic media, these take the form:

$$\mathbf{D} = \varepsilon \mathbf{E}, \tag{2.5}$$

$$\mathbf{B} = \mu \mathbf{H}, \tag{2.6}$$

where ε is the permittivity and μ is the permeability of the medium. In free space, these reduce to ε_0 and μ_0, with $\varepsilon_0 = 8.854 \times 10^{-12}$ F/m and $\mu_0 = 4\pi \times 10^{-7}$ H/m [72].

Maxwell's equations show that time-varying electric and magnetic fields are intrinsically coupled, enabling the propagation of electromagnetic waves. The propagation velocity is determined by the medium properties:

$$v = \frac{1}{\sqrt{\mu\varepsilon}},$$

which highlights the fundamental role of material parameters in shaping electromagnetic behavior [71].
Variations in permittivity directly influence wave velocity, wavelength, and field distribution. In practical materials, especially lossy and dispersive media, these properties deviate from ideal conditions and significantly affect electromagnetic wave behavior. The implications of such material responses, particularly in biological media, will be discussed in the following sections.

2.1.2 Permittivity and Conductivity in Biological Media

Biological tissues are characterized by frequency-dependent electromagnetic properties, primarily permittivity $\varepsilon(\omega)$ and conductivity $\sigma(\omega)$, which govern electromagnetic wave propagation and attenuation within the medium [69, 70].
A convenient representation is the complex permittivity:

$$\varepsilon^* = \varepsilon' - j\varepsilon'' = \varepsilon' - j\frac{\sigma}{\omega},$$

where ε' represents the energy storage capability of the material, while the imaginary component accounts for conductive losses [57].
The presence of conductivity leads to attenuation of electromagnetic waves as energy is dissipated within the medium. As a result, both the effective wavelength and propagation characteristics differ significantly from those in free space. The wavelength in a dielectric medium can be approximated as:

$$\lambda = \frac{1}{f\sqrt{\mu\varepsilon'}},$$

indicating that higher permittivity results in shorter wavelengths [71].
These frequency-dependent and lossy properties are particularly important for biological media, where high permittivity and non-negligible conductivity result in strong attenuation and dispersion effects. Such characteristics play a fundamental role in determining wave penetration and energy distribution in tissue, as discussed in subsequent sections [69].

2.2 Electromagnetic Wave Propagation and Interaction with Biological Media

The design of microwave imaging systems for head bleeding detection requires a clear understanding of how electromagnetic waves propagate through and interact with heterogeneous biological tissues.

This section presents the underlying physical mechanisms, beginning with wave propagation in dielectric media, followed by frequency-dependent material behavior and attenuation effects. Based on these principles, the implications for antenna coupling, detection, and electromagnetic environment control are discussed.

2.2.1 Wave Propagation in Biological Media

Electromagnetic wave propagation in biological media is fundamentally governed by the dieletric properties introduced in Section 2.1. In contrast to free space, where waves propagate at the speed of light c, the phase velocity v_{ph} in a material medium depends on its permittivity [71].
By expressing the material parameters in terms of their relative values, $\varepsilon = \varepsilon_r \varepsilon_0$ and $\mu = \mu_r \mu_0$, the phase velocity can be written as:

$$v_{\mathrm{ph}} = \frac{1}{\sqrt{\mu\varepsilon}} = \frac{c}{\sqrt{\mu_r \varepsilon_r}}. \tag{2.7}$$

For most biological tissues, the relative permeability is approximately unity ($\mu_r \approx 1$), and therefore wave propagation is primarily determined by the relative permittivity ε_r. Due to the high water content of soft tissues, typically around 70–80%, biological media exhibit relatively large permittivity values compared to free space [69].
As a consequence, the phase velocity of electromagnetic waves in tissue is significantly reduced. For example, at frequencies around 1 GHz, the propagation velocity in brain tissue is several times lower than in free space, leading to a corresponding reduction in wavelength. The wavelength in the medium is given by:

$$\lambda = \frac{v_{\mathrm{ph}}}{f} = \frac{1}{f\sqrt{\mu\varepsilon}}, \tag{2.8}$$

indicating that higher permittivity results in shorter wavelengths within the tissue[72]. This wavelength compression has important implications for electromagnetic field distribution and spatial resolution in imaging applications. At the same time, the altered propagation characteristics introduce additional complexity due to the heterogeneous and lossy nature of biological tissues. These effects, including frequency-dependent behavior and attenuation mechanisms, are further examined in the following sections.

2.2.2 Dielectric Relaxation and Conductivity Mechanisms

The interaction between electromagnetic waves and biological tissue is governed by the complex relative permittivity, defined as $\varepsilon_r^*(\omega) = \varepsilon_r' - j\varepsilon_r''$, which captures both energy storage and loss mechanisms [69]. In the microwave frequency range, biological tissues exhibit dispersive behavior and cannot be accurately modeled as simple resistive or capacitive media.
To account for this behavior, the dielectric response of biological tissues is commonly described using the Cole-Cole model [70, 57]:

$$\varepsilon_r^*(\omega) = \varepsilon_\infty + \frac{\varepsilon_s - \varepsilon_\infty}{1 + (j\omega\tau)^{1-\alpha}} + \frac{\sigma_{dc}}{j\omega\varepsilon_0}. \tag{2.9}$$

Here, ε_s and ε_∞ denote the static and high-frequency permittivity limits, respectively, τ represents the characteristic relaxation time, and α accounts for the broadening of the relaxation spectrum. The term σ_{dc} represents the ionic conductivity, which contributes to dielectric losses.
This formulation highlights that both polarization effects and electrical conduction contribute to the complex permittivity. These mechanisms lead to frequency-dependent attenuation and dispersion of electromagnetic waves in biological tissues, which are examined in the following section.

2.2.3 Penetration Depth in Lossy Dielectrics

This subsection focuses on how electromagnetic waves attenuate in biological tissues and how deeply they can penetrate.
At microwave frequencies, biological tissues behave as lossy dielectrics, where both conduction current density and displacement current density are comparable [69, 57]. As a result, simple skin depth approximations used for highly conductive materials are not suitable for accurately describing wave propagation in tissue.
The penetration depth δ is defined as the distance at which the field amplitude decreases to $1/e$ of its initial value, and can be expressed as [71]:

$$\delta = \frac{1}{\omega} \left\{ \frac{\mu\varepsilon}{2} \left[\sqrt{1 + \left(\frac{\sigma}{\omega\varepsilon}\right)^2} - 1 \right] \right\}^{-1/2}. \tag{2.10}$$

This expression shows that increasing frequency leads to reduced penetration depth due to higher dielectric losses. Consequently, electromagnetic waves are attenuated more rapidly in biological tissue at higher frequencies.
This behaviour limits the ability of signals to reach deeper regions within the medium and must be considered when selecting the operating frequency.

2.2.4 Impact of Dielectric Properties on Antenna Performance

This subsection examines how the dielectric properties of biological media influence antenna performance, particularly in terms of coupling efficiency and energy loss.
The performance of an antenna operating in or near biological tissue is governed by the electromagnetic properties of the surrounding medium, primarily the relative permittivity ε_r and the electrical conductivity σ. These parameters define the propagation environment and influence both the coupling of electromagnetic energy into the medium and the resonance behaviour of the antenna. In general, ε_r affects impedance matching at material interfaces, while σ contributes to energy dissipation within the medium.
To better understand these effects, wave interaction at an interface can be considered. The electromagnetic response of the medium is described using the complex permittivity,

$$\varepsilon^* = \varepsilon - j\frac{\sigma}{\omega}, \tag{2.11}$$

and the corresponding intrinsic impedance,

$$\eta = \sqrt{\frac{\mu}{\varepsilon^*}}. \tag{2.12}$$

These parameters determine the reflection and transmission of electromagnetic waves at the interface [71, 68]. As electromagnetic waves propagate, energy is dissipated due to conductive losses, which reduces the effective signal strength. Therefore, both permittivity and conductivity must be considered when evaluating antenna performance in biological environments.
The dielectric properties of the medium influence both how efficiently energy is coupled into the tissue and how much of that energy is preserved during propagation. Accurate characterization of these properties is therefore essential for reliable system modelling and performance evaluation.

2.2.5 Detection Principle

The detection of intracranial hemorrhage relies on the contrast in dielectric properties. Because the magnetic permeability of biological tissues is negligible ($\mu_r \approx 1$), imaging contrast arises almost exclusively from differences in complex permittivity (ε^*) and conductivity (σ).
The signal chain for detection can be conceptualized as follows[65]:

1. **Injection:** The antenna injects electromagnetic fields into the head volume.
2. **Interaction:** The head acts as a lossy propagation medium in which propagating electromagnetic fields undergo attenuation and scattering due to dielectric losses within the tissue.
3. **Scattering:** A hemorrhage introduces a local anomaly in dielectric parameters. This perturbation redistributes the electromagnetic field, altering the scattering and absorption patterns.
4. **Observation:** These internal changes manifest as variations in the measured signals at the antenna ports, which can be represented in different ways. A common representation is through scattering parameters (S-parameters), which describe the relationship between incident and reflected waves at the antenna ports[71].

It is important to consider the interaction between electromagnetic fields and the biological environment. Microwave signals in the 0.5–1.5 GHz range oscillate on nanosecond time scales (10^{-9} s), which are several orders of magnitude faster than typical biological processes such as thermal diffusion or neural activity. As a result, stroke detection is based on how these high-frequency fields are scattered and perturbed by dielectric contrasts within the tissue. In particular, hemorrhagic regions introduce local variations in permittivity and conductivity, thereby disrupting the propagation of electromagnetic waves through the head.

2.2.6 Electromagnetic Environment Control

Multipath interference is a major factor that degrades signal quality in microwave imaging systems. In microwave imaging systems, effective control of the electromagnetic environment is critical for isolating signals of interest from environmental clutter [66]. In the proposed configuration, multipath components—particularly those propagating along the head surface or outside the region of interest—introduce unwanted reflections, signal distortion, and reconstruction artifacts, thereby reducing imaging accuracy.

A dielectric coupling medium is employed to suppress multipath propagation and improve signal coupling. Specifically, the medium is applied to the back and lateral sides of the antenna array [67]. This design serves two key purposes. First, it reduces impedance discontinuities at the air–skin interface, thereby suppressing surface-wave propagation along the head. Second, it enhances electromagnetic coupling between the antennas and biological tissues, enabling more efficient energy transmission into the imaging region.

The suppression of reflections and multipath components relies on impedance matching and controlled attenuation. From an electromagnetic perspective, minimizing reflections requires proper matching across different media interfaces. Unlike conventional single-layer absorbers, which typically exhibit narrowband performance, a lossy dielectric medium provides broadband attenuation suitable for ultra-wideband (UWB) operation. The conductivity of the medium introduces controlled energy dissipation, which helps attenuate unwanted multipath signals while preserving sufficient penetration into the target region.

The electromagnetic properties of the coupling medium can be tailored to optimize system performance. By adjusting parameters such as effective permittivity and conductivity through material composition, it is possible to achieve a trade-off between impedance matching, attenuation, and practical manufacturability. This flexibility allows the proposed approach to improve the electromagnetic environment without requiring complex multilayer absorber structures.

Overall, the proposed design effectively suppresses multipath interference while maintaining signal penetration, making it well-suited for wearable UWB microwave imaging systems.

2.3 Antenna Theory and Design Constraints in the Context of Head Imaging

Designing antennas for biomedical microwave imaging requires a fundamental departure from conventional free-space communication systems. Instead of radiating into an open environment, the antenna array must couple electromagnetic energy into a highly complex, heterogeneous, and lossy dielectric load—the human head. The main purpose of this section is to establish the theoretical framework governing these electromagnetic interactions, directly linking fundamental parameters to the selection, synthesis, and evaluation of the coupling gel and brain tissue phantoms developed in this project.

2.3.1 Radiation Mechanism and Dielectric Loading Effects

Fundamentally, antenna radiation originates from accelerated charge carriers. When a time-varying current oscillates on a conductor, the associated electric and magnetic fields decouple from the source and propagate outward. In on-body microwave medical imaging, this radiation mechanism is heavily modified by the immediate dielectric environment. The wave propagation is governed by the effective wavelength, λ_{eff}, which scales inversely with the square root of the medium's relative permittivity:

$$\lambda_{\text{eff}} \approx \frac{\lambda_0}{\sqrt{\varepsilon_r}} \tag{2.13}$$

where λ_0 is the free-space wavelength and ε_r is the relative permittivity of the surrounding medium [68].

In this project, this "dielectric loading" effect serves a dual purpose. When the antenna is immersed in or coupled to a high-permittivity matching gel, its electrical size increases relative to the wavelength. This compresses the physical dimensions required for resonance, enabling the design of a compact, high-density antenna array capable of surrounding the patient's head [73]. However, this proximity also alters the near-field reactive energy storage and can degrade radiation efficiency due to conductive losses (σ) in the tissues. Therefore, characterizing the exact ε_r and σ of our synthesized carbon-loaded silicone coupling gel is critical to balancing antenna miniaturization against transmission efficiency.

2.3.2 Input Impedance, Reactive Loading, and Gel Optimization

The electrical interface of the antenna is characterized by its complex input impedance, $Z_{\text{in}}(\omega)$, defined as:

$$Z_{\text{in}}(\omega) = R_{\text{in}}(\omega) + jX_{\text{in}}(\omega) \tag{2.14}$$

The resistive component, $R_{\text{in}} = R_{\text{rad}} + R_{\text{loss}}$, represents the sum of the radiation resistance (R_{rad}) and the loss resistance (R_{loss}) originating from both the antenna structure and the dissipative surrounding tissues. The reactive component, X_{in}, represents the non-propagating energy stored in the antenna's near field.

Resonance occurs when the capacitive and inductive reactances cancel out ($X_{\text{in}} \approx 0$). In head imaging, direct contact with biological tissue severely perturbs this balance. High-permittivity coupling layers induce severe capacitive loading, shifting the resonant frequency downward [74]. Consequently, the matching gel cannot be treated merely as a passive acoustic or physical buffer; it is an integral components of the antenna's resonant circuit. By adjusting the formulations of our carbon-loaded silicone composites, we aim to stabilize Z_{in} and ensure predictable resonant behavior when the array is deployed against the head.

2.3.3 Impedance Matching and Signal Reflection Metrics

To maximize power transfer from the transceiver (typically designed with a characteristic impedance $Z_0 = 50\,\Omega$) into the brain tissue, the antenna impedance must be precisely matched to the load. The quality of this match is quantified by the complex reflection coefficient, Γ:

$$\Gamma = \frac{Z_{\text{in}} - Z_0}{Z_{\text{in}} + Z_0} \tag{2.15}$$

For Ultra-Wideband (UWB) microwave imaging, which relies on short, transient pulses to achieve high spatial resolution, the primary metric for bandwidth performance is the Return Loss (RL), expressed in decibels:

$$\text{RL} = -20 \log_{10} |\Gamma| \tag{2.16}$$

A standard criterion for operational bandwidth is $\text{RL} \geq 10\,\text{dB}$ (corresponding to a Voltage Standing Wave Ratio $\text{VSWR} \leq 2:1$), implying that at least 90% of the incident power is accepted into the medium [75].
Because Z_{in} is highly sensitive to the spatial distribution of ε_r and σ, tracking variations in RL serves as our primary experimental method to evaluate the efficacy of different matching gel formulations. A well-optimized gel minimizes reflections at the skin interface, ensuring that the bulk of the RF energy penetrates deeper into the skull.

2.3.4 Skin Effect, Attenuation, and Phantom Design Target

The skin effect describes the rapid attenuation of electromagnetic waves as they propagate through a conductive, lossy medium. The penetration depth (or skin depth, δ), defined as the distance at which the field amplitude decays to $1/e$ (approximately 37%) of its surface value, is given by:

$$\delta = \sqrt{\frac{2}{\omega \mu \sigma}} \tag{2.17}$$

where ω is the angular frequency, μ is the magnetic permeability, and σ is the electrical conductivity of the medium [76].
This relationship highlights the fundamental trade-off in microwave diagnostics: higher frequencies (ω) provide better spatial resolution but severely restrict the penetration depth due to increased tissue conductivity. In intracranial hemorrhage detection, the wave must cross highly attenuating layers to reach the deep-seated target tissue. This constraint dictates the specific composition of the water-salt-sugar solutions used for our brain tissue phantoms. By carefully tuning the salt concentration and sugar concentration, we can accurately replicate the lossy environment of human brain tissues, allowing us to experimentally verify whether the antenna array can overcome the skin effect to detect internal dielectric anomalies.

2.3.5 Near-Field Distribution and Energy Coupling Efficiency

In head imaging applications, antenna performance is entirely dominated by near-field interactions rather than far-field radiation patterns. In this regime, the electromagnetic field consists primarily of evanescent, non-propagating components, and

the overriding objective is to optimize the spatial concentration of energy within the region of interest.
Because a substantial portion of the transmitted power is dissipated as heat in the superficial layers of the head, conventional far-field metrics are irrelevant. Instead, system performance must be evaluated in terms of near-field coupling efficiency. This efficiency is maximized by implementing a matching medium whose dielectric properties closely mirror those of human tissue[77]. Utilizing our synthesized carbon-composite gel minimizes the permittivity contrast at the antenna-tissue boundary, mitigating reflection losses and steering more electromagnetic energy into the intracranial region to improve overall diagnostic sensitivity.

2.4 Computational Electromagnetics and Numerical Modelling

Accurate modeling of microwave imaging systems requires reliable numerical solutions of Maxwell's equations in heterogeneous and lossy biological environments. In this work, simulations were performed using CST Studio Suite (Dassault Systèmes), which is based on the Finite Integration Technique (FIT) [78, 79]. Both time-domain and frequency-domain solvers were employed to ensure numerical accuracy and cross-validation of the results.

2.4.1 Time-Domain Solver

The primary simulations of the ultra-wideband (UWB) antenna array were performed using the time-domain solver based on the Finite Integration Technique (FIT). FIT provides a consistent discretization of Maxwell's equations in integral form and enables broadband analysis from a single excitation [80].
This makes it particularly suitable for UWB imaging systems, where the response over a wide frequency range must be evaluated efficiently. In addition, the time-domain approach accurately captures transient electromagnetic wave propagation and attenuation in lossy biological tissues, which is essential for modelling signal penetration and scattering in head imaging scenarios.

2.4.2 Frequency-Domain Solver

To validate the time-domain results, a frequency-domain solver based on the Finite Element Method (FEM) was also employed. FEM discretizes Maxwell's equations over an unstructured mesh, allowing accurate modelling of complex geometries and material interfaces.
This is particularly advantageous for representing curved antenna structures and heterogeneous anatomical features in the head phantom. Although FEM is computationally more expensive for broadband analysis, it provides highly accurate steady-state solutions at selected frequencies, making it suitable for verification and detailed frequency analysis [81].

2.5 Summary

This chapter has presented the fundamental theoretical framework underlying microwave imaging in biological tissues, with a particular focus on head imaging applications.
First, the key electromagnetic principles governing wave propagation in lossy and heterogeneous media were introduced, including Maxwell's equations, dielectric properties of biological tissues, and penetration depth limitations. These concepts establish the physical basis for understanding how microwave signals interact with the human head.
Next, the interaction between antennas and biological media was discussed, highlighting the impact of dielectric loading, impedance matching, and near-field energy coupling. In particular, the role of the matching medium was emphasized as a critical factor in reducing reflection losses and improving power transmission into the tissue.
Finally, numerical modelling techniques based on the Finite Integration Technique (FIT) and Finite Element Method (FEM) were introduced to enable accurate simulation of electromagnetic fields in complex anatomical environments. These methods provide the computational basis for evaluating antenna performance and optimizing system design.
Overall, this chapter establishes the theoretical and numerical foundation for the design and evaluation of antenna systems and matching media in the subsequent chapters.

3

Methods

3.1 Experimental Procedures and Numerical Simulations

The significant challenge in microwave-based intracranial hemorrhage detection is the significant impedance mismatch between the antenna array and the human head. This mismatch triggers strong reflections and multipath signals that can obscure the desired scattering data, leading to artifacts in the reconstructed images and potential misdiagnosis. To mitigate these effects and ensure efficient signal coupling, a specialized matching medium must be introduced between the antennas and the target.

The following experimental campaign was designed to validate the proposed matching strategy through a systematic investigation of coupling media properties. The study first examines different gel materials with varying dielectric properties to evaluate their impact on electromagnetic wave propagation, with particular emphasis on the suppression of multipath signals.

Based on this analysis, the dielectric properties that provide the most effective reduction in unwanted signal propagation are identified. A matching gel is then formulated and measured to achieve these target properties.

Finally, the performance of the designed material is assessed through numerical simulation, where scattering parameters of the antenna array are evaluated to verify the effectiveness of the proposed matching strategy.

3.1.1 Dielectric Characterization

The relative permittivity (ε_r') and conductivity (σ) of the fabricated gel samples were characterized using a commercial dielectric assessment kit (DAK, SPEAG, Zurich, Switzerland). This system utilizes the open-ended coaxial probe technique to measure dielectric properties over the frequency range of interest (0.5–2.0 GHz). Prior to measurement, the system was calibrated using a three-load standard procedure (open, short, and deionized water) to ensure accuracy. The temperature of the samples was monitored and maintained at room temperature (25°C) during the acquisition process to avoid thermal drift.

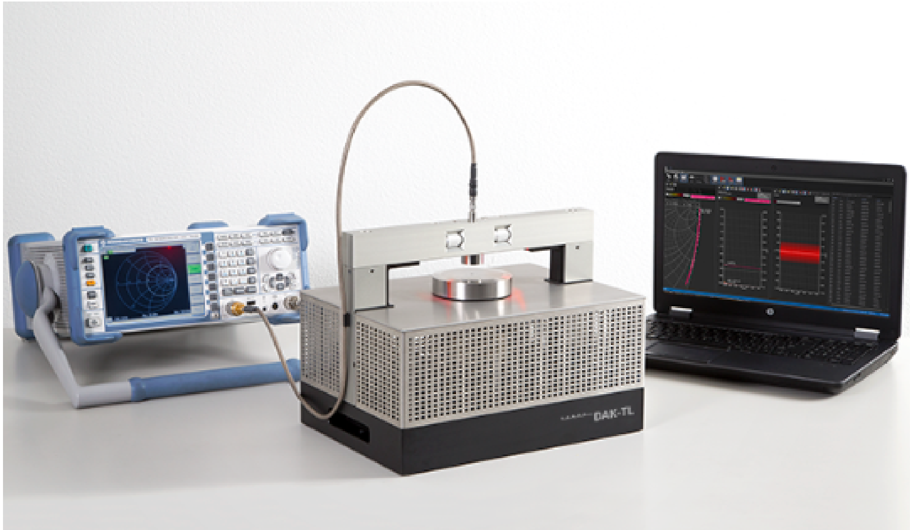

Figure 3.1: Experimental setup showing the SPEAG Dielectric Assessment Kit (DAK) used for characterizing the dielectric properties of the gel samples[89].

3.1.2 Antenna Array Measurements

The scattering parameters (S-parameters) of the fabricated antenna system were measured using a multiport Vector Network Analyzer (ZNBT8, Rohde & Schwarz, Munich, Germany). The ZNBT8 allows for the simultaneous characterization of up to 16 ports, which is essential for evaluating the coupling effects and transmission coefficients in the antenna array without the need for external switching matrices. The VNA was calibrated using a standard full N-port TOSM (Through, Open, Short, Match) calibration kit to de-embed the effects of the coaxial cables and connectors.

Figure 3.2: Measurement setup utilizing the 16-port Vector Network Analyzer (ZNBT8, Rohde & Schwarz) for full-matrix S-parameter characterization of the antenna array [90].

3.2 Material Design, Fabrication, and Characterization

The development of effective coupling and absorbing materials requires a systematic workflow that spans material selection, composite formulation, and experimental characterization. This section outlines the rationale behind the chosen material systems, the preparation of both commercial and laboratory-synthesized composites, and the procedures used to fabricate and evaluate the samples.

3.2.1 Material Selection and Design Rationale

To guide the material design, existing dielectric materials were first examined from the perspective of their achievable permittivity–conductivity combinations.

High-permittivity composites developed for energy storage and embedded capacitor applications typically aim to maximize dielectric constant while suppressing dielectric loss to improve energy efficiency. For example, polymer–ceramic systems incorporating $BaTiO_3$ or $CaCu_3Ti_4O_{12}$ fillers can achieve moderate relative permittivity ($\varepsilon_r \approx 7$–12), but their loss tangents are usually kept below 10^{-2}, resulting in very low effective electrical conductivity [24, 25, 26]. Such materials are therefore unsuitable for applications requiring appreciable electromagnetic attenuation.

In contrast, dielectric materials used in high-frequency electronics, such as printed circuit board (PCB) substrates and microwave ceramics, are specifically engineered to exhibit low permittivity and ultra-low loss in order to preserve signal integrity and maintain high quality factors. Typical systems, including PTFE-based laminates and low-loss ceramic dielectrics, exhibit $\varepsilon_r < 4$ and extremely small dielectric loss [28, 31]. These characteristics inherently imply negligible conductivity, making them incompatible with applications where absorption rather than transmission is desired.

On the other end of the spectrum, highly conductive composites developed for electromagnetic interference (EMI) shielding rely on the formation of percolating conductive networks using fillers such as carbon black, graphene, or metal particles. Once the percolation threshold is reached, electrical conductivity increases sharply, often at the expense of controlled dielectric behavior [33]. Although such materials can provide strong attenuation, their electromagnetic response is typically dominated by surface reflection rather than volumetric absorption, and their permittivity is difficult to tune independently.

Interestingly, biological tissues provide a natural example of materials exhibiting both high permittivity and moderate conductivity, primarily due to their high water content and ionic conduction mechanisms. Reported values for human tissues show relative permittivity on the order of tens and conductivities in the range of several S/m in microwave frequencies [69]. However, these properties are intrinsically linked to their fluidic composition and are difficult to reproduce in stable, solid, and mechanically robust materials suitable for practical engineering applications.

These observations reveal a clear material design gap: existing systems typically optimize either high permittivity with low loss, or high conductivity with limited dielectric tunability, but rarely achieve both simultaneously. Therefore, achieving a balance between permittivity enhancement and controlled conductivity remains a

key challenge in the design of solid electromagnetic absorbers.
To address this challenge, conductive polymer composites based on silicone matrices loaded with carbon fillers were selected as a promising approach. Such systems enable continuous tuning of dielectric properties through filler concentration, while maintaining mechanical flexibility, processability, and structural stability [84]. This makes them well-suited for developing solid coupling materials tailored for microwave absorption and multipath mitigation.

3.2.2 Composite Formulation and Commercial Materials

To evaluate and develop suitable materials, both commercial absorbers and laboratory-synthesized composites were investigated. The inclusion of commercial materials provides benchmark references for assessing the electromagnetic performance of the developed composites.
The commercial absorber materials used in this study were sourced from Gomeasure, SWELEX, and Laird. The selected products include polymer–magnetic absorbers, ferrite-based panels, elastomer/foam absorbers, and carbon-loaded foams, covering a representative range of commercially available microwave absorbing technologies. A summary of the commercial materials, including manufacturers and material types, is provided in Table 3.1.

Table 3.1: Summary of Commercial Absorber Materials Used in This Study.

Material Name	Manufacturer	Material Type
SEA-ELP[92]	Gomeasure	Thin magnetic polymer absorber
SEA-ELS[92]	Gomeasure	Soft magnetic polymer absorber
SEA-FE [91]	Gomeasure	Ferrite-based absorber
ABS-LFE-SA[93]	SWELEX	Elastomer/foam absorber
LS-30 (Eccosorb)[94]	Laird	Carbon foam absorber

In addition to commercial materials, a range of composite materials were synthesized in this study. The conductive fillers included iron powder, copper powder, and carbon-based materials such as graphite, C45, and VULCAN carbon black. The silicone matrices used were C25 condensation-cure silicone, Dragon Skin silicone, Ecoflex silicone, and a food-grade silicone[95]. All materials were used as received without further chemical modification.

3.2.3 Sample Preparation

Composite samples were prepared by mixing conductive fillers with silicone matrices at different weight fractions ($wt\%$). Various formulations were explored to investigate how the filler type, matrix properties, and loading levels influence the resulting electromagnetic behavior.
For each sample, the required amounts of filler and silicone were first weighed. The components were then mixed until a uniform dispersion was obtained, with care taken to reduce particle agglomeration. Depending on the viscosity of the silicone, additional manual mixing was applied when necessary to improve homogeneity.

The mixtures were subsequently poured into custom-designed molds. To minimize trapped air, the samples were degassed in a vacuum chamber prior to curing. All samples were then cured at room temperature for approximately 24 hours until fully solidified.

After curing, the samples were removed from the molds and used for dielectric and electromagnetic measurements. The detailed compositions are summarized in Table 3.2.

Table 3.2: Detailed compositions of the synthesized composites. The sample code indicates the filler type and loading level. "Filler" refers to the conductive additive, "Matrix" is the silicone base material, and "Filler Content" specifies the weight percentage of filler in the composite.

Sample Code	**Filler**	**Matrix**	**Filler Content** ($wt\%$)
Graphite/Dragon_skin-30	Graphite	Dragon_skin	30
Graphite/Dragon_skin-45	Graphite	Dragon_skin	45
Graphite/C25-30	Graphite	C25	30
Graphite/C25-45	Graphite	C25	45
Iron/Ecoflex-50	Iron Powder	Ecoflex	50
Copper/Ecoflex-50	Copper Powder	Ecoflex	50
C45/Ecoflex-6	C45	Ecoflex	6
VULCAN/Ecoflex-5	VULCAN	Ecoflex	5
VULCAN/Ecoflex-10	VULCAN	Ecoflex	10
VULCAN/Ecoflex-15	VULCAN	Ecoflex	15
VULCAN/Ecoflex-20	VULCAN	Ecoflex	20
VULCAN/Foodgrade-5	VULCAN	Food-grade [95]	5
VULCAN/Foodgrade-10	VULCAN	Food-grade [95]	10
VULCAN/Foodgrade-15	VULCAN	Food-grade [95]	15
VULCAN/Foodgrade-20	VULCAN	Food-grade [95]	20
VULCAN/C25-15	VULCAN	C25	15
VULCAN/C25-20	VULCAN	C25	20

3.3 Simulations and Image Reconstructions

This section describes the simulation setup, signal processing, and image reconstruction framework used to localize the hemorrhagic target. The electromagnetic modelling and CST simulation geometry are first introduced to define the forward-propagation environment. The workflow then consists of preprocessing measured S-parameters, transforming them into the time domain, and reconstructing the image using a beamforming algorithm. An enhanced DMAS approach is further introduced to improve robustness and image quality under complex propagation conditions.

3.3.1 Simulation Geometry

To evaluate the electromagnetic interaction between the antenna array and the biological target, a simplified planar model was developed using CST Studio Suite. The simulation setup, illustrated in Fig. 3.3, comprises a central dielectric block representing the intracranial environment surrounded by a four-element antenna array.

The head phantom is modeled as a rectangular dielectric volume with cross-sectional dimensions of 190 × 150 mm and dielectric properties characterized by a relative permittivity of $\varepsilon_r = 40$ and an electrical conductivity of $\sigma = 0.4$ S/m. This simplified geometry was selected to approximate the average electrical cross-section of the human head while maintaining computational efficiency for parametric sweeps. As depicted in Fig. 3.3a, the four antenna elements are positioned orthogonally around the phantom, ensuring direct contact with the surface to emulate a realistic wearable scenario.

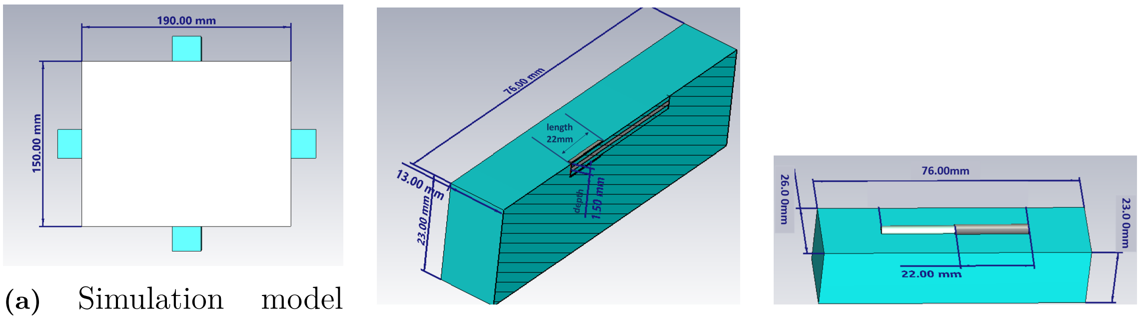

(a) Simulation model overview **(b)** Cross-section view **(c)** Front view

Figure 3.3: Geometry of the antenna element. (a) Simulation model overview. (b) Cross-section view showing the slot and internal structure with the slot length ($L = 22$ mm) and depth ($D = 1.5$ mm) indicated. (c) Front view of the antenna block with the slot length ($L = 22$ mm).

The detailed geometry of a single radiating element is presented in Fig. 3.3b and Fig. 3.3c . The antenna structure is embedded within a solid matching gel layer (shown in blue), which provides mechanical support and facilitates impedance matching to the high-permittivity phantom.

In the baseline configuration, the gel block has dimensions of 26 mm (width), 23 mm (height), and 76 mm (length). A critical objective of this study is the optimization of these geometric parameters to enhance signal penetration.

3.3.2 Preprocessing and Time-Domain Conversion

The measured scattering parameters (S-parameters) are first preprocessed to suppress background interference and enhance target contrast. Specifically, a differential signal is constructed between the normal and bleeding scenarios:

$$S_{\text{diff}}(f) = S_{\text{normal}}(f) - S_{\text{bleeding}}(f) \tag{3.1}$$

This subtraction removes the contributions from the background tissue that are common to both scenarios, thereby isolating the scattered response associated with the hemorrhagic target.
The resulting frequency-domain signals are then transformed into the time domain using an inverse fast Fourier transform (IFFT). To ensure a physically meaningful real-valued time-domain waveform, a two-sided spectrum is constructed by mirroring the measured positive-frequency components prior to transformation.

3.3.3 DMAS Beamforming Algorithm

After obtaining the time-domain signals, a beamforming algorithm is required to reconstruct the spatial image. Image reconstruction is performed using the Delay-Multiply-and-Sum (DMAS) beamforming algorithm. For each imaging pixel located at position $\mathbf{r}$, the propagation delay between a transmitting antenna i and a receiving antenna j is given by:

$$\tau_{ij}(\mathbf{r}) = \frac{\|\mathbf{r} - \mathbf{r}_i\| + \|\mathbf{r} - \mathbf{r}_j\|}{v} \tag{3.2}$$

where $\mathbf{r}_i$ and $\mathbf{r}_j$ denote the antenna positions, and v is the wave velocity in the medium.
The corresponding time-domain signals are sampled at the calculated delays. Unlike conventional Delay-and-Sum (DAS), which linearly sums delayed signals, DMAS introduces nonlinear correlation by multiplying signal pairs:

$$I(\mathbf{r}) = \sum_{i=1}^{N} \sum_{j=i+1}^{N} s_i(\tau_i(\mathbf{r})) \cdot s_j(\tau_j(\mathbf{r})) \tag{3.3}$$

This nonlinear operation enhances coherent scattering components while suppressing incoherent noise, resulting in improved image contrast.

3.3.4 Weighted DMAS Enhancement

To further improve reconstruction robustness, a distance-based weighting scheme is introduced. The weighting coefficient for each antenna pair is defined as:

$$w_{ij} = \max(0, \alpha - d_{ij}) \tag{3.4}$$

where d_{ij} is the Euclidean distance between antennas i and j, and α is a predefined threshold. This weighting prioritizes signal pairs with stronger mutual coupling while suppressing less reliable contributions.
Additionally, a temporal integration window is introduced to improve robustness against delay estimation errors and signal fluctuations:

$$I(\mathbf{r}) = \sum_{t=\tau-W}^{\tau+W} \sum_{i<j} w_{ij}\, s_i(t) \cdot s_j(t) \tag{3.5}$$

where W denotes the half-window length. This integration relaxes the requirement for precise time alignment by accumulating signal contributions over a short temporal interval. As a result, it mitigates the impact of discretization and propagation uncertainties, while also providing a smoothing effect that enhances reconstruction stability.

3.3.5 Imaging Setup

The imaging system consists of eight antennas arranged around a cylindrical head phantom, as illustrated in Fig. 3.4. The antennas are positioned in a partial circular configuration along one side of the phantom, representing a practical limited-view scenario.

Two target positions are tested. In the central case (Fig. 3.4(a)), the bleeding inclusion is placed near the middle of the phantom. In the lateral case (Fig. 3.4(b)), the inclusion is placed closer to the boundary and nearer to the antenna array. This allows us to evaluate how the imaging system performs under both symmetric and asymmetric conditions.

The antennas operate inside a coupling medium with $\varepsilon_r = 40$ and $\sigma = 7$ S/m. These values come from the material characterization in the previous section and were selected to provide good signal penetration while keeping losses manageable.

For each antenna pair, the simulation records the complex transmission coefficient $S_{ij}(f)$ over the operating frequency range. These S-parameters form the dataset used for image reconstruction. Both the central and lateral target positions are simulated using the same procedure.

A background simulation is first performed using the phantom without any inclusion. This reference dataset is then subtracted from the dataset containing the bleeding inclusion. The resulting difference highlights only the changes caused by the target and removes the static contribution from the antennas, coupling medium, and phantom.

The reconstruction is carried out on a fixed cross-sectional plane at $z = 0.20$ m, which corresponds to the height of the inclusion. The calibrated data are processed using the imaging algorithm to produce a map showing where the dielectric contrast is located inside the phantom.

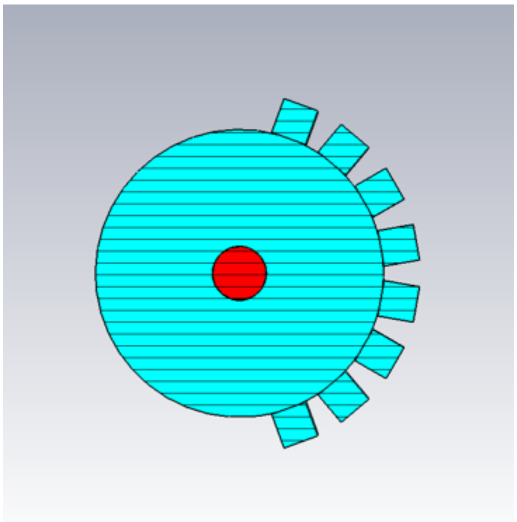

(a) Central target configuration

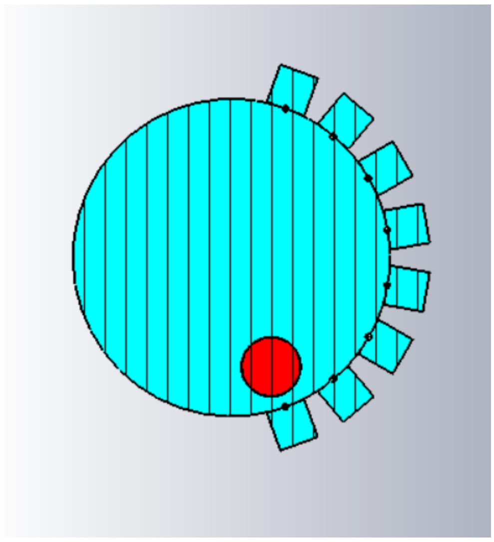

(b) Lateral target configuration

Figure 3.4: Imaging setup and target configurations. (a) Central inclusion located near the center of the cylindrical phantom. (b) Lateral inclusion positioned close to the boundary and antenna array, representing an asymmetric scenario. The vertical and horizontal lines are the default coordinate axes displayed by CST and do not represent any physical structures in the model. Both configurations are shown on the reconstruction plane at $z = 0.20$ m, which corresponds to the cross-sectional slice used for image reconstruction.

4

Results

This chapter presents the simulation results, material characterization outcomes, and reconstructed images obtained in this study. Building upon the modelling and experimental procedures described in Chapter 3, the results are organized into three main parts. First, a comprehensive parametric study is performed to evaluate how the coupling medium's conductivity, permittivity, and geometry influence antenna behaviour and electromagnetic field propagation. Second, the dielectric properties of commercial absorbers and synthesized composite materials are characterized to assess their suitability as solid coupling media. Finally, the impact of the optimized material on imaging performance is demonstrated through reconstructed images using the DMAS algorithm. Together, these results provide a systematic evaluation of the proposed antenna–gel configuration and its effectiveness for suppressing multipath interference in microwave-based brain imaging.

4.1 Simulation Results and Parametric Study

4.1.1 Analysis of Coupling Medium Conductivity

The parametric study in this section is performed using the same simulation geometry described in Section 3 and illustrated in Fig. 3.3a. This setup consists of the four-element antenna array arranged around the planar head phantom with the baseline gel block dimensions defined in the Methods chapter.
To investigate the impact of the coupling medium's loss characteristics on the antenna performance, a parametric sweep of the medium's electrical conductivity (σ) was conducted. The relative permittivity (ε_r) was maintained at a constant value of 40, while the conductivity was varied from 3 S/m to 9 S/m in steps of 2 S/m. This range was selected to emulate potential variations in biological tissue properties or coupling gel formulations.

4.1.1.1 Scattering parameters

The reflection coefficient (S_{11}) for different conductivity values is shown in Fig. 4.1. The results illustrate how increasing conductivity affects both the resonance behaviour and the overall coupling performance.
First, a gradual reduction in resonance depth is observed as conductivity increases. At $\sigma = 3$ S/m, the antenna exhibits a well-defined resonance with a minimum below -20 dB around 1.3 GHz. As the conductivity increases to $\sigma = 5$ and 7 S/m, the minimum becomes less pronounced, rising to approximately -15 dB and -13 dB

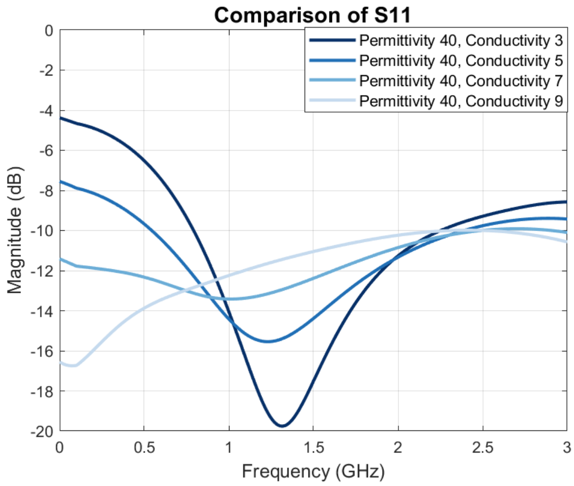

Figure 4.1: Comparison of simulated S_{11} parameters for varying medium conductivity ($\sigma = 3, 5, 7, 9$ S/m) with fixed permittivity ($\varepsilon_r = 40$).

respectively. At $\sigma = 9$ S/m, the resonance is significantly weakened, with the S_{11} curve becoming relatively flat and remaining close to -10 dB across a wide frequency range.

Second, a slight shift of the resonance towards lower frequencies can be observed as conductivity increases. However, this shift is relatively small compared to the change in resonance depth, indicating that conductivity primarily affects the strength of resonance rather than its frequency location.

The observed behaviour can be explained by increased conductive losses in the medium[71, 68]. As conductivity increases, a larger portion of the electromagnetic energy is dissipated as heat, reducing the amount of energy available for radiation and resonance. This leads to weaker and broader S_{11} responses, as seen in the higher-conductivity cases.

It is important to note that a low S_{11} value over a wide frequency range does not necessarily indicate efficient antenna performance. In highly conductive media, the reduced reflection can result from energy absorption rather than effective radiation into the medium. Consequently, high conductivity can degrade system performance by reducing the signal strength.

The signal transmission efficiency is evaluated using the S_{21} and S_{41} parameters, as shown in Fig. 4.2.

A clear reduction in transmission magnitude is observed as the conductivity increases for both transmission paths. For S_{21}, the transmission level decreases from approximately -70 dB at $\sigma = 3$ S/m to below -90 dB for $\sigma = 9$ S/m across the main frequency band. A similar trend is observed for S_{41}, where the signal level drops significantly as conductivity increases.

This consistent reduction across both near (S_{21}) and farther (S_{41}) transmission paths indicates that the observed behaviour is primarily governed by material losses rather than geometrical effects.

The attenuation can be attributed to increased conductive losses in the medium. As conductivity increases, a larger portion of the electromagnetic energy is dissipated as heat during propagation, reducing the power that reaches the receiving antennas

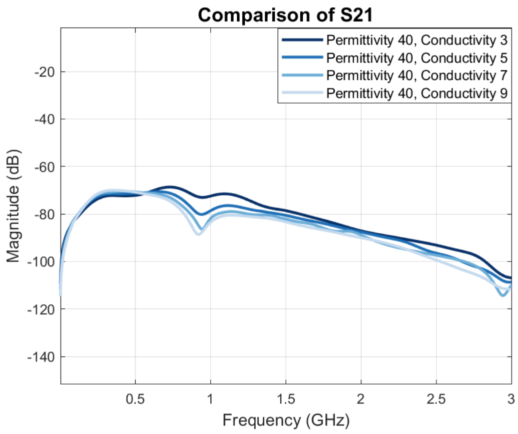

(a) S_{21} parameter.

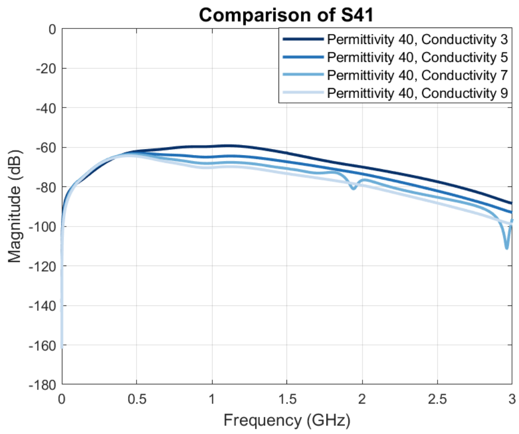

(b) S_{41} parameter.

Figure 4.2: Comparison of transmission coefficients, (a) S_{21} and (b) S_{41}, illustrating signal attenuation levels for different conductivity values ($\sigma = 3, 5, 7, 9$ S/m).

[71].
Consequently, although higher conductivity may help suppress unwanted multipath signals, it also leads to significant signal attenuation, which can degrade the overall system performance by limiting the detectable signal strength.

4.1.1.2 Volume Loss in GEL

To further evaluate energy dissipation within the coupling medium, the total volume loss in the gel was analysed, as shown in Fig. 4.3. CST computes the total volume loss by integrating the power–loss density over the gel volume. The loss density is defined as

$$p_{\text{loss}} = \tfrac{1}{2}\sigma|E|^2,$$

where σ is the conductivity and E is the electric field magnitude[71]. CST evaluates this quantity throughout the gel and integrates it to obtain the total dissipated power at each frequency. This parameter represents the electromagnetic power converted into heat within the medium and provides insight into how much energy is lost during propagation.
Several key trends can be observed. First, the overall volume loss increases with conductivity, indicating that more electromagnetic energy is dissipated in higher-conductivity media. For example, the $\sigma = 9$ S/m case consistently exhibits higher loss compared to $\sigma = 3$ S/m across the frequency range.
Second, at lower conductivity values (e.g., $\sigma = 3$ S/m), a pronounced peak is observed around 1 GHz, suggesting stronger field concentration and resonance effects within the medium. As conductivity increases, this peak gradually diminishes and the response becomes flatter, indicating that the resonance behaviour is suppressed. This behaviour can be explained by conductive losses in the medium. The power dissipation is proportional to conductivity and the square of the electric field magnitude [57]. While increasing conductivity enhances the intrinsic loss mechanism, it also reduces the electric field strength inside the medium due to increased impedance

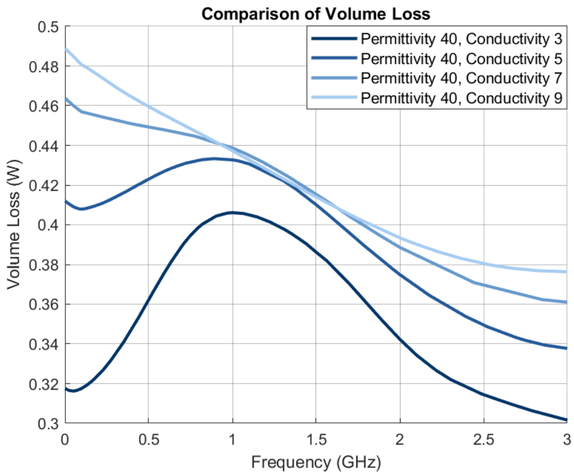

Figure 4.3: Simulated total volume loss (power dissipation) in the gel phantom for varying conductivity values ($\sigma = 3, 5, 7, 9$ S/m).

mismatch and attenuation. As a result, the total volume loss does not increase proportionally with conductivity and instead shows a more gradual variation.
These results are consistent with the trends observed in the S-parameter analysis. Higher conductivity leads to increased energy dissipation and reduced transmission, but also suppresses resonance behaviour, highlighting the trade-off between signal attenuation and multipath reduction.

4.1.1.3 Field Distribution

To visualize the physical mechanism of signal attenuation and energy confinement, the electric field (E-field) distributions are compared in Fig. 4.4.
The visual comparison confirms the numerical findings regarding signal penetration. For the lower conductivity case ($\sigma = 3$ S/m), distinct wavefronts are visible propagating deeply into the phantom. In contrast, for the high conductivity case ($\sigma = 9$ S/m), the high-intensity field is confined to the immediate vicinity of the antenna elements. The field strength decays rapidly within a few millimeters, entering the low-intensity region (blue) before reaching the target area.
This behavior is consistent with the skin effect described in Section theory, where higher conductivity leads to a reduced penetration depth. Consequently, although increased conductivity enhances the absorption of the incident wave, it significantly limits field propagation, rendering the system ineffective for detecting deep-seated intracranial hemorrhages.
However, the field distributions also reveal a secondary and beneficial effect in terms of lateral propagation. In the proposed microwave imaging array, antennas are arranged circumferentially, and excessive lateral radiation is undesirable as it leads to strong mutual coupling between adjacent elements, which can obscure weak scattering signals from the brain.
As shown in Fig. 4.4, the lower conductivity case ($\sigma = 3$ S/m) exhibits widely spreading lateral wavefronts, which are likely to cause significant interference between neighboring antennas. In contrast, as the conductivity increases beyond 5

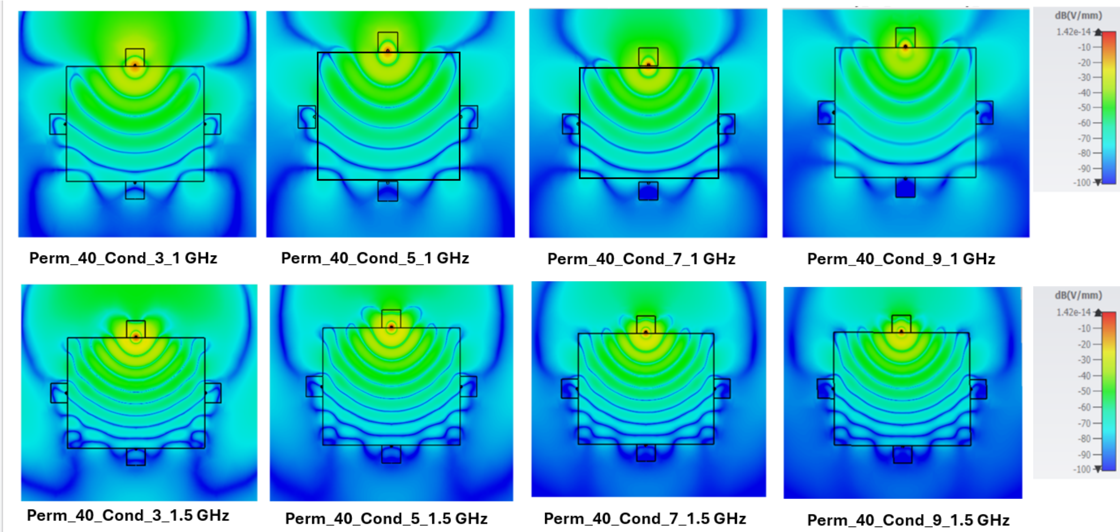

Figure 4.4: Simulated E-field distributions for materials with $\varepsilon_r = 40$ at two frequencies. The top row shows all cases at 1 GHz, while the bottom row shows the corresponding cases at 1.5 GHz. Within each row, conductivity increases from left to right ($\sigma = 3,\ 5,\ 7,\ 9$ S/m), illustrating how higher conductivity leads to stronger attenuation.

S/m, the lateral surface waves are effectively attenuated by the lossy gel, resulting in electromagnetic energy being tightly confined near the antenna aperture. This suggests that higher conductivity ($\sigma > 5$ S/m) can improve channel isolation by suppressing lateral wave propagation.

4.1.2 Analysis of Coupling Medium Permittivity

While conductivity dictates the dissipative properties of the medium, the relative permittivity (ε_r) fundamentally governs the wave propagation velocity and energy storage capacity. To understand its influence, a parametric sweep of ε_r was performed (ranging from 30 to 90) while maintaining a constant conductivity of $\sigma = 5$ S/m.

4.1.2.1 Scattering parameters

The reflection coefficients (S_{11}) for different permittivity values are shown in Fig. 4.5. Two main effects can be observed: a shift in the resonant frequency and a change in the resonance depth.

First, as the relative permittivity increases from 30 to 90, the resonant frequency shifts progressively towards lower frequencies. For example, the resonance moves from approximately 1.3–1.4 GHz at $\varepsilon_r = 30$ to around 1.0 GHz at $\varepsilon_r = 80$ and below 1.0 GHz for $\varepsilon_r = 90$.

Second, the resonance becomes deeper as permittivity increases. The minimum S_{11} value decreases from around -14 dB for $\varepsilon_r = 30$ to below -20 dB for $\varepsilon_r = 90$, indicating improved impedance matching and stronger coupling between the antenna and the surrounding medium.

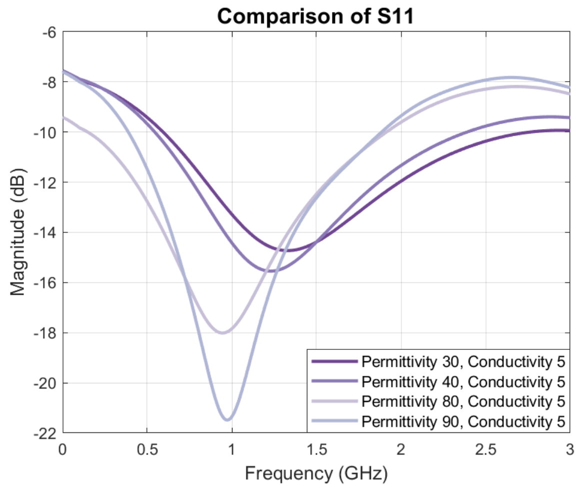

Figure 4.5: Simulated S_{11} parameters for varying relative permittivity ($\varepsilon_r = 30, 40, 80, 90$) with fixed conductivity ($\sigma = 5$ S/m).

These observations can be explained by the reduction in wavelength within the dielectric medium. The guided wavelength is inversely proportional to the square root of the permittivity,

$$\lambda_g = \frac{c}{f\sqrt{\varepsilon_r}}, \tag{4.1}$$

which increases the electrical length of the antenna for a fixed physical size. As a result, the resonance condition is achieved at lower frequencies, consistent with the observed shift[71].

Overall, increasing permittivity enhances impedance matching and reduces reflection, but also shifts the operating frequency. Therefore, the dielectric properties of the coupling medium must be carefully selected to align the antenna resonance with the desired imaging band.

To evaluate the system's performance, two distinct transmission paths were analyzed based on the antenna array configuration. (S_{21}) refers to the transmission coefficient measured at the diametrically opposite antenna (receiving through the brain tissue), while (S_{41}) refers to the coupling measured at the adjacent antenna (receiving surface waves). The simulation results for varying permittivity values are presented side-by-side in Fig. 4.6.

As shown in Fig. 4.6(a), the signal penetration (S_{21}) shows a moderate dependence on the medium's permittivity. At 1 GHz, the case with $\varepsilon_r = 40$ (second darkest curve) exhibits relatively high transmission efficiency, maintaining a level around -77 dB. In contrast, increasing the permittivity to $\varepsilon_r = 90$ results in a reduction of approximately 4 dB (dropping to -81 dB).

This behaviour can be partially attributed to the fact that the permittivity of brain tissue is close to 40, which reduces dielectric contrast and reflection losses at the tissue interface. However, this trend is not consistently observed across all frequencies, where the relative ordering of the curves may change, suggesting that the overall dependence on permittivity is relatively weak.

This limited sensitivity may be related to the system configuration, where a significant portion of the coupling medium is located behind the monopole antenna,

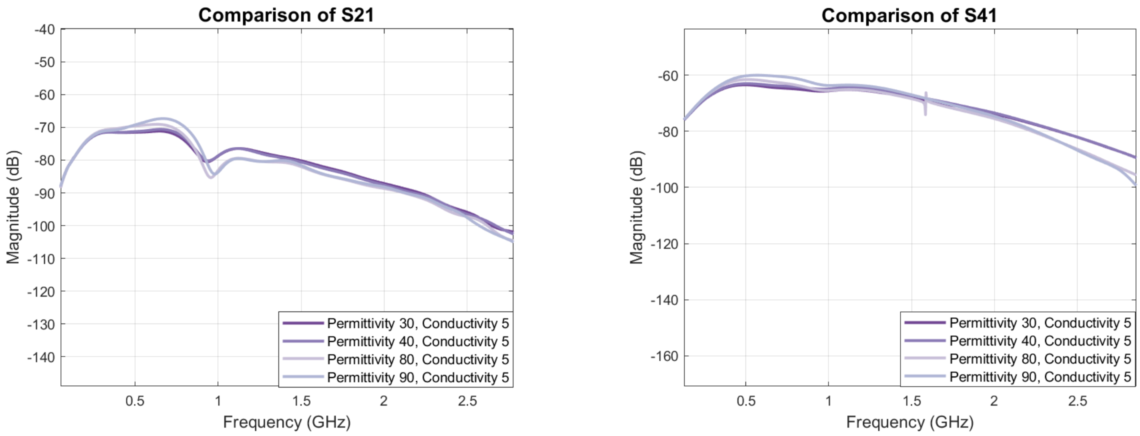

Figure 4.6: Simulated scattering parameters for varying permittivity values ($\varepsilon_r = 30, 40, 80, 90$) with fixed conductivity ($\sigma = 5$ S/m). (a) S_{21} measured at the opposite port indicates signal penetration efficiency, while (b) S_{41} measured at the adjacent port represents lateral coupling levels.

reducing its influence on the forward propagation toward the target.

Regarding isolation, Fig. 4.6(b) illustrates the signal(S_{41}) between adjacent ports. The coupling levels remain consistently low (below -60 dB) across all permittivity cases. It is noteworthy that while permittivity significantly impacts the transmission efficiency (S_{21}), the variations in S_{41} are relatively minor. This suggests that the isolation performance is primarily governed by the medium's conductivity (absorption of lateral waves) and physical antenna spacing, making the system's interference immunity robust against permittivity fluctuations in the coupling gel.

Based on the trade-off between miniaturization (frequency shift) and signal penetration (S_{21}), a permittivity in the range of $\varepsilon_r = 40$ is identified as the optimal choice, offering the best compromise between impedance matching and signal integrity.

4.1.2.2 Volume Loss in GEL

The total volume loss for different permittivity values is shown in Fig. 4.7. Several trends can be observed from the results.

First, at lower frequencies (below approximately 1 GHz), the volume loss increases with permittivity. For example, the cases with $\varepsilon_r = 80$ and 90 exhibit noticeably higher loss compared to $\varepsilon_r = 30$ and 40, indicating that more electromagnetic energy is dissipated within the gel.

Second, all curves exhibit a peak around 1 GHz, which corresponds to stronger field concentration or resonance within the medium. This behaviour is consistent with the resonance observed in the S_{11} results.

However, beyond approximately 1.2–1.5 GHz, the trend begins to reverse. At higher frequencies, larger permittivity values no longer produce higher losses; instead, the volume loss decreases more rapidly for $\varepsilon_r = 80$ and 90, and the curves gradually converge.

This behaviour can be explained by the influence of permittivity on the electromagnetic field distribution rather than direct energy dissipation. Although permittivity

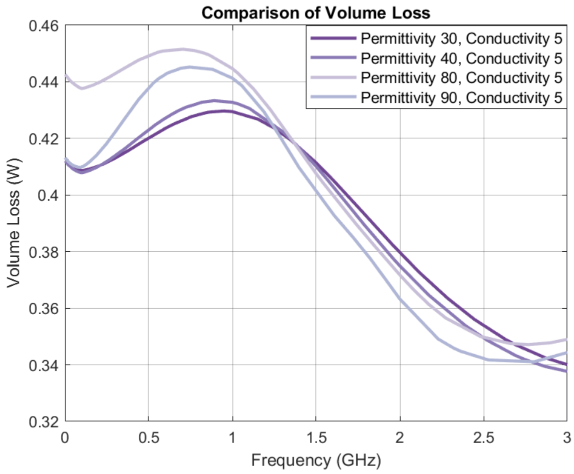

Figure 4.7: Total volume loss within the gel for varying permittivity values. Note the increasing trend despite constant conductivity.

itself does not cause loss, it affects impedance and field confinement within the medium. At lower frequencies, higher permittivity promotes field concentration, leading to increased energy dissipation. At higher frequencies, however, the reduced wave impedance results in stronger reflection at the interface, limiting the amount of energy entering the medium[57].

Consequently, the total volume loss depends not only on the material conductivity, but also on how permittivity influences the internal field distribution and energy coupling into the gel.

4.1.2.3 Field Distribution

To visualize the impact of permittivity on wave propagation characteristics, the electric field distributions at 1 GHz and 1.5GHz are compared in Fig. 4.8.

First, the field distributions exhibit a noticeable change in radiation characteristics as the relative permittivity increases. A clear increase in backward radiation is observed, with stronger fields appearing behind the antenna (i.e., away from the phantom), indicating enhanced reflection due to impedance mismatch.

Second, in the lateral direction, the field initially becomes more directive as the permittivity increases from $\varepsilon_r = 30$ to $\varepsilon_r = 40$, with reduced energy spreading along the sides of the antenna. However, this trend is not monotonic. At higher permittivity values ($\varepsilon_r = 80$ and 90), the lateral field components become more pronounced again. This can be attributed to the increased impedance contrast between the coupling medium and the phantom, which leads to stronger reflections and redistribution of energy near the interface.

Overall, these observations indicate that excessively high permittivity does not simply improve field confinement, but instead introduces strong reflections that degrade efficient energy transmission and lead to unintended field spreading. In contrast, moderate permittivity ($\varepsilon_r = 40$) achieves a more favorable balance, with reduced lateral spreading and more effective coupling of energy into the phantom.

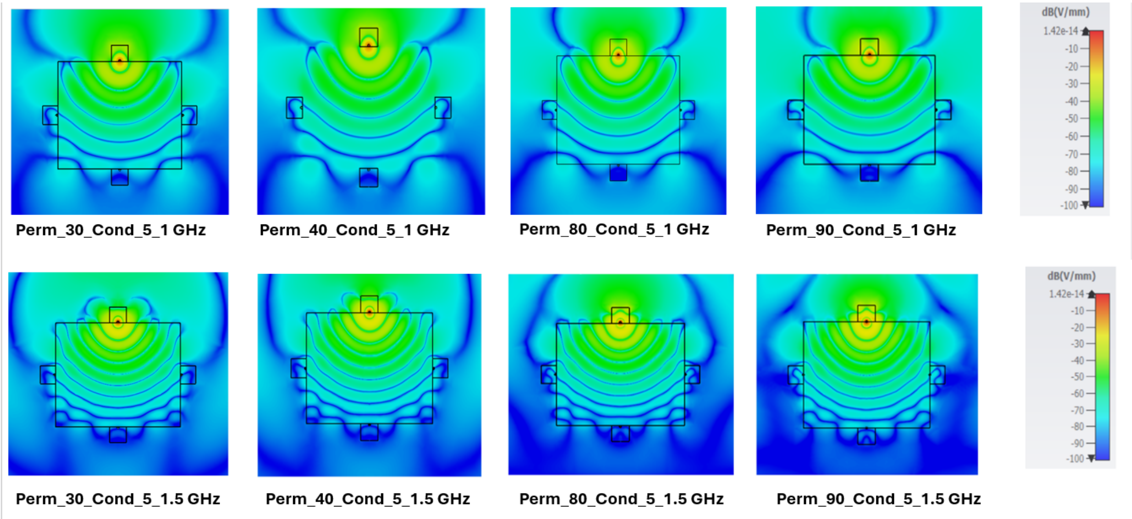

Figure 4.8: Simulated E-field distributions at 1 GHz and 1.5GHz. The top panel ($\varepsilon_r = 40$) exhibits a wavelength matched to the antenna dimensions, while the bottom panel ($\varepsilon_r = 90$) demonstrates higher reflection.

4.1.3 Analysis of Coupling Medium Dimensions

To determine the optimal geometry of the coupling medium, a parametric study was conducted on four distinct gel sizes. The goal was to mitigate multipath wave while ensuring the internal signal penetration remains within the detectable dynamic range of the measurement instrument. The analysis focuses on the impact of gel thickness (H), width (W), and length (L) on the antenna's near-field behavior, as illustrated in Fig. **??**.

4.1.3.1 Scattering parameters

The reflection coefficient (S_{11}) results are shown in Fig. 4.9.

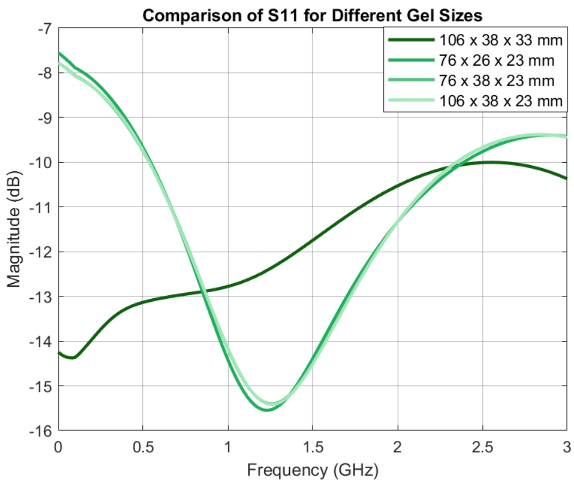

Figure 4.9: Simulated S_{11} for different gel dimensions.The dimensions are denoted as Length $\times$ Width $\times$ Thickness.

The simulation reveals that the gel thickness is the critical parameter governing the resonant frequency by comparing the darkest line and the brightest line. As observed, variations in length (L) (compare the first line with the third line) and width (W) (compare the second line with the third line) have a negligible effect on the S_{11} profile. However, the thickness (H) significantly shifts the operating point. To ensure effective coupling, the resonance peak must be aligned within the target band of 0.5–1.5 GHz. If the gel is too thick, the resonance may shift out of this range. Conversely, if it is too thin, it fails to buffer the high-permittivity skin reflection. Therefore, the thickness is constrained primarily by this impedance matching requirement.
The (S_{21}) and (S_{41}) are presented side-by-side in Fig. 4.10.

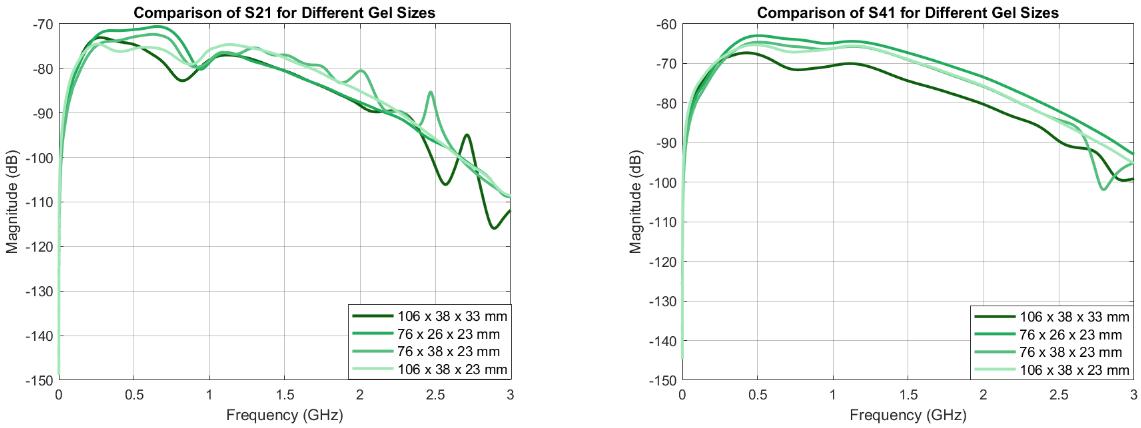

(a) Transmission (S_{21}).

(b) Isolation (S_{41}).

Figure 4.10: Impact of gel dimensions on (a) signal penetration S_{21} and (b) S_{41}.

A clear trend is observed: increasing the gel dimensions, particularly thickness and width, leads to lower S-parameter magnitudes.
For the gel thickness, a thicker layer introduces a longer propagation path within the lossy medium. As a result, the electromagnetic wave experiences greater attenuation due to dielectric losses, leading to a reduction in the transmitted signal (S_{21}). This explains the significant drop in signal level observed for the largest gel configuration in Fig. 4.10(a). While a thicker gel is effective in suppressing unwanted surface waves, it can excessively attenuate the desired penetrating signal. If the signal becomes too weak, it may fall below the sensitivity threshold of the measurement system, making reliable detection impossible.
For the gel width, increasing the lateral dimension reduces mutual coupling between adjacent antennas. This occurs because the electromagnetic waves must travel a longer path through the lossy gel, where they are partially absorbed, thereby reducing signal (S_{41}), as shown in Fig. 4.10(b). However, this reduction in coupling is accompanied by an overall decrease in signal strength due to additional losses.
Therefore, increasing gel dimensions provides improved isolation but at the expense of signal penetration. This highlights a critical trade-off: while larger gel sizes are beneficial for suppressing interference, excessively large dimensions degrade the useful signal. An optimal gel size must therefore balance sufficient isolation and adequate signal strength for reliable detection.

4.1.3.2 Field Distribution

The electric field distributions for different gel widths are shown in Fig. 4.11. The results illustrate how the gel width influences the propagation and confinement of electromagnetic waves around the antenna.

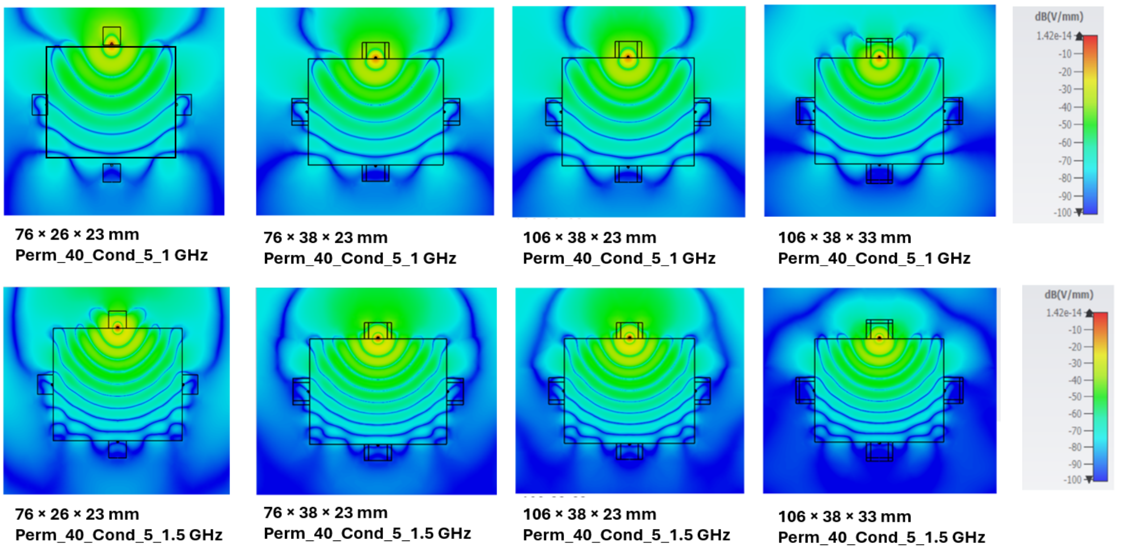

Figure 4.11: E-field distributions for different gel widths. Wider gels effectively absorb lateral waves, preventing energy leakage to the surrounding environment and neighboring antennas.

For the narrower gel configurations, strong lateral propagation of the electromagnetic waves can be observed. The field contours extend beyond the gel region, indicating that a portion of the radiated energy leaks towards the surrounding environment and neighboring antenna elements.
As the gel width increases, the lateral spreading of the field is significantly reduced. The field becomes more confined within the gel region, and the intensity outside the gel boundary decreases. In the widest configurations, the electromagnetic waves are largely contained within the gel, with minimal leakage to the sides.
This behaviour can be attributed to the lossy nature of the gel medium, which absorbs laterally propagating waves and suppresses surface propagation [57]. As a result, increasing the gel width improves isolation between antenna elements and reduces unwanted multipath interactions.
Overall, a wider gel provides better electromagnetic shielding and energy confinement, which is beneficial for minimizing interference within the antenna array.

4.1.4 Analysis of Antenna Dimensions

The physical dimensions of the antenna, specifically the radiating metal length (L) and the immersion depth (D), as illustrated in Fig. **??**, significantly influence the system's performance. The antenna length primarily dictates the radiated power and resonance frequency, while the depth determines the coupling efficiency and the power absorbed by the coupling gel. To understand how these parameters affect wave propagation near the head, we analyzed the scattering parameters and electric field distributions under varying antenna lengths and depths.

4.1.4.1 Scattering Parameters

The simulated reflection coefficients (S_{11}) for different antenna dimensions are shown in Fig. 4.12. The results highlight the influence of antenna length (L) and immersion depth (D) on the resonance behaviour.

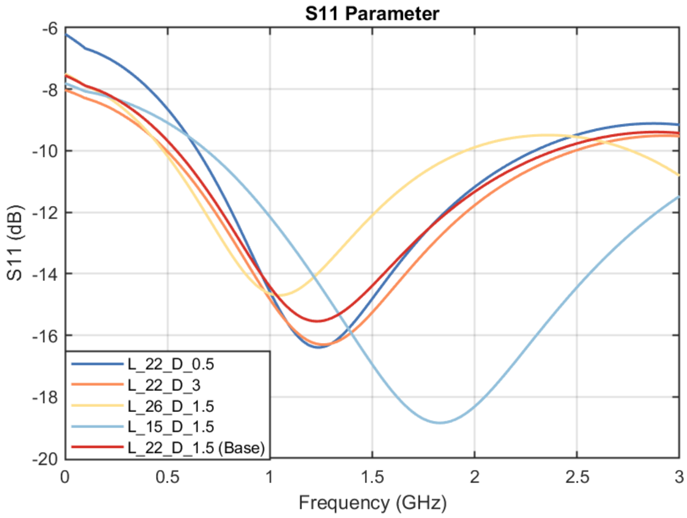

Figure 4.12: Simulated reflection coefficient (S_{11}) for different antenna dimensions. The length (L) significantly shifts the resonance frequency, while the depth (D) has a negligible effect on the resonance frequency.

First, the antenna length has a significant impact on the resonant frequency. As L increases, the resonance shifts towards lower frequencies. For example, the configuration with $L = 15$ exhibits a resonance around 1.8–2.0 GHz, while increasing the length to $L = 22$ shifts the resonance to approximately 1.2–1.3 GHz. A further increase to $L = 26$ moves the resonance close to 1.0 GHz.

Second, the resonance depth also varies with antenna length. The $L = 15$ case produces the deepest resonance (below -18 dB), while longer antennas show slightly shallower responses. This indicates that antenna length affects not only the resonant frequency but also the impedance matching quality.

In contrast, the immersion depth (D) has a negligible effect on the resonance frequency. For configurations with the same antenna length ($L = 22$), varying D from 0.5 to 3 results in nearly identical resonance positions, with only minor differences in the magnitude of S_{11}.

These results show that antenna length is the primary parameter for tuning the operating frequency, while immersion depth mainly influences the coupling strength rather than the resonance location. Therefore, to align the antenna with the target operating band of 0.5–1.5 GHz, the antenna length must be carefully optimized, while depth can be adjusted to control signal coupling.

The transmission (S_{21}) and isolation (S_{41}) coefficients are presented side-by-side in

Fig. 4.13. The results show how antenna dimensions influence both signal penetration and coupling between elements.

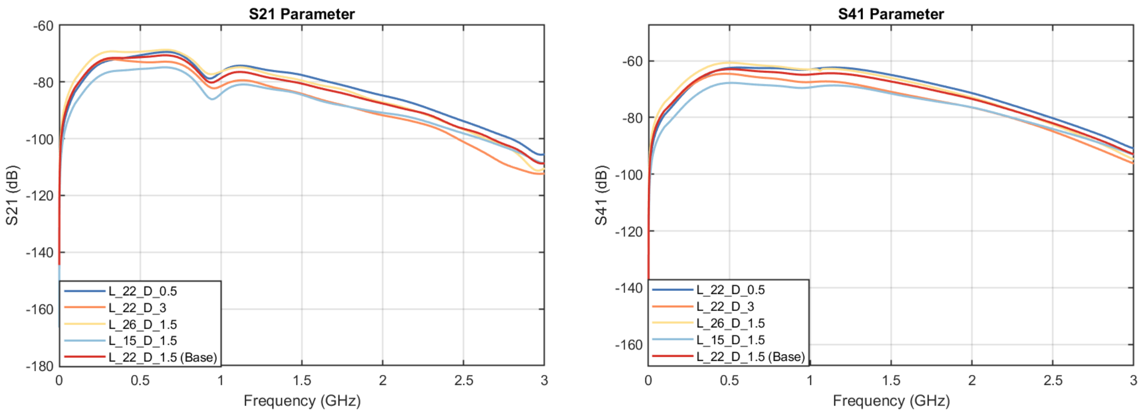

(a) Transmission (S_{21}). **(b)** Isolation (S_{41}).

Figure 4.13: Impact of antenna dimensions on (a) signal penetration (S_{21}) and (b) (S_{41}).

For the transmission coefficient (S_{21}), a clear variation in signal level is observed across the different configurations. The case with $L = 22$ and $D = 0.5$ exhibits the highest transmission, with values around -70 dB in the main frequency band. In contrast, the shorter antenna ($L = 15$) shows significantly lower transmission, with a reduction of approximately 10–15 dB. This indicates that antenna length has a strong impact on the amount of energy delivered into the medium.
The effect of immersion depth is also evident. Comparing configurations with the same antenna length ($L = 22$), the shallower placement ($D = 0.5$) consistently provides higher transmission than deeper placement ($D = 3$). This suggests that a deeper antenna experiences additional attenuation due to the longer propagation path within the lossy gel.
A similar trend is observed in the isolation coefficient (S_{41}). Configurations with higher transmission also exhibit higher coupling levels, indicating stronger interaction between antenna elements. Although the variations in S_{41} are smaller, the overall behaviour follows the same pattern as S_{21}.
These results demonstrate that antenna geometry influences both signal penetration and inter-element coupling. Increasing the antenna length and reducing the immersion depth improves energy delivery into the medium, but may also increase unwanted coupling, highlighting a trade-off in antenna design.

4.1.4.2 Field Distribution

To visualize the radiation mechanism and isolation, the electric field distributions for different antenna configurations are shown in Fig. 4.14.
Clear differences in field intensity and propagation behaviour can be observed across the configurations. For the longer antenna ($L = 26$), a stronger electric field is generated around the radiating element, with a larger high-intensity region and more pronounced wavefronts propagating into the surrounding medium. In contrast, the

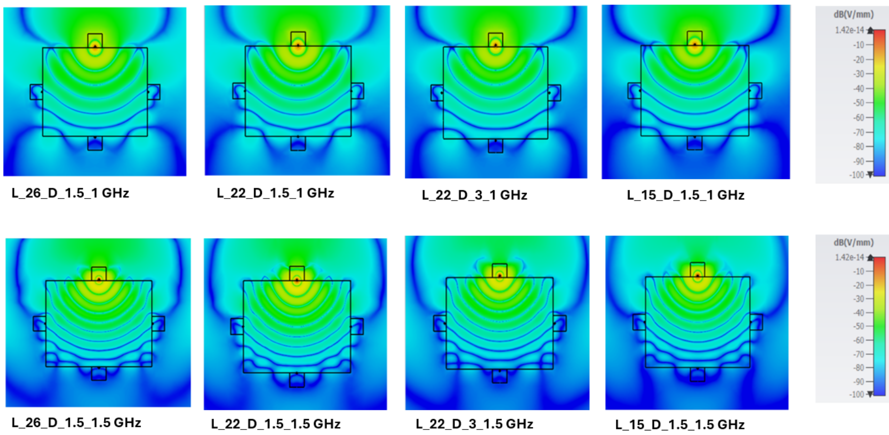

Figure 4.14: E-field distributions for different antenna dimensions. The field intensity increases with antenna length, confirming improved radiation efficiency.

shorter antenna ($L = 15$) exhibits a noticeably weaker field, with reduced propagation distance and less defined wave patterns.

The effect of antenna length is therefore evident in both the field magnitude and the spatial extent of wave propagation. Longer antennas produce a stronger and more sustained field distribution, enabling more efficient energy transfer into the medium. The impact of immersion depth (D), however, is less significant in terms of overall field distribution. Comparing configurations with the same antenna length ($L = 22$), variations in depth result in only minor changes in field intensity, while the overall propagation pattern remains largely unchanged.

These observations are consistent with the S-parameter analysis, where antenna length was found to strongly influence transmission, while depth mainly affects coupling strength rather than the radiation pattern.

4.2 Dielectric Characterization of Candidate Materials

This section presents the dielectric characterization of all investigated material systems. All dielectric data in this section were obtained using a SPEAG Dielectric Assessment Kit (DAK). For each material, the sample was placed in contact with the open-ended coaxial probe, and the instrument measured the real permittivity (ϵ_r') and electrical conductivity (σ) at multiple frequencies within the microwave range. This procedure was applied consistently to all commercial, metal, graphite, and carbon-black composites.

4.2.1 Commercial Absorbing Materials

First, commercially available electromagnetic absorbing materials were evaluated. The four commercial absorber materials evaluated here correspond to the products listed in Table 3.1 in Chapter 3, namely SEA-ELP, SEA-ELS, ABS-LFE-SA, and LS-30. As shown in Fig. 4.15, these materials display a wide range of dielectric

properties. While some samples exhibit relatively high permittivity (up to approximately 48), their electrical conductivity remains low, generally below 0.3 S/m across the measured frequency range.
Overall, none of the tested commercial materials simultaneously achieve the target permittivity ($\epsilon_r \approx 40$) and conductivity ($\sigma \approx 7$). These results indicate that, despite being designed for wave absorption, the evaluated products do not meet the specific electromagnetic requirements for mitigating multipath signal interference in this study.

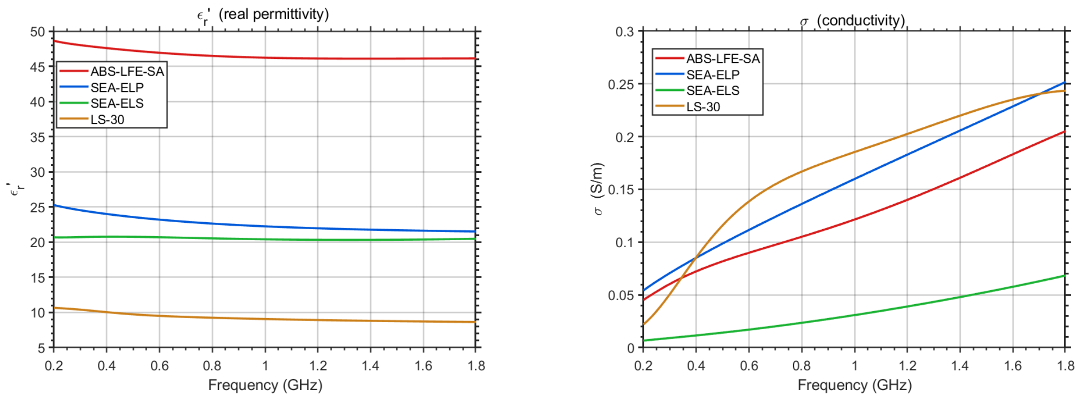

(a) permittivity ϵ_r' **(b)** conductivity σ

Figure 4.15: Real permittivity (ϵ_r') and electrical conductivity (σ) of four commercial electromagnetic absorbing materials measured over the 0.2–1.8 GHz frequency range. The left plot shows ϵ_r' as a function of frequency, and the right plot shows σ for the same materials across the same frequency range.

4.2.2 Metal Powder Materials

In addition to commercial products, metal-based composites were investigated to examine whether high intrinsic conductivity can be translated into effective composite performance. Both iron and copper powders were incorporated into the Dragonskin silicone matrix at a high filler loading of 50 wt%. The metal-based composites analyzed here correspond to the iron- and copper-loaded samples listed in Table 3.2, specifically Iron/Ecoflex-50 and Copper/Ecoflex-50. As shown in Fig. 4.16, the resulting composites exhibit relatively low electrical conductivity across the measured frequency range (0.2–1.8 GHz), remaining close to zero and not exceeding approximately 0.018 S/m, despite a slight increase with frequency.
This behavior is unexpected given the intrinsically high conductivity of metal fillers, suggesting that a continuous conductive network was not established within the silicone matrix even at high loading. In contrast, the relative permittivity remains moderate, with copper-based composites ($\epsilon_r' \approx 9.1$–9.3) showing slightly higher values than iron-based composites ($\epsilon_r' \approx 8.1$–8.3), although both are far below the target permittivity of approximately 40. Overall, these results demonstrate that metal–silicone composites at 50 wt% loading fail to simultaneously achieve the required conductivity and permittivity, rendering them unsuitable for mitigating multipath signal interference in this study.

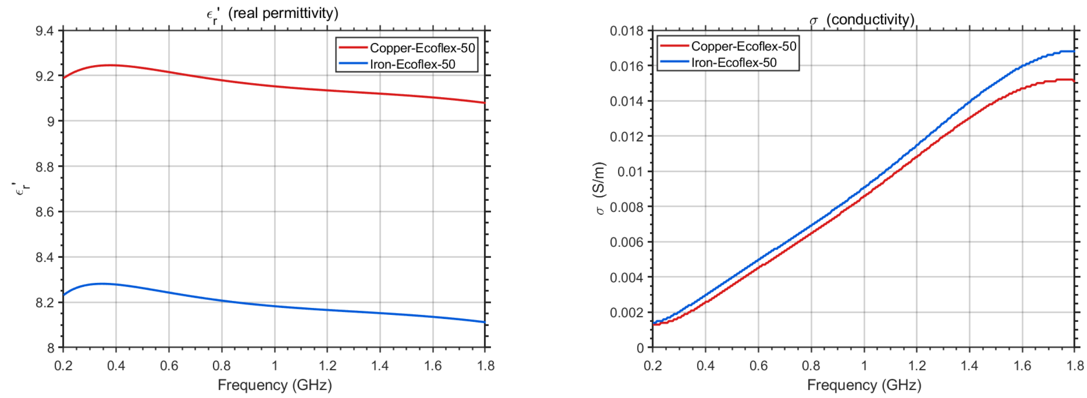

(a) permittivityϵ_r' **(b)** conductivity σ

Figure 4.16: Real permittivity (ϵ_r') and electrical conductivity (σ) of two metal silicone composites (IRON_Ecoflex_50% and COPPER_Ecoflex_50%) measured over the 0.2–1.8 GHz frequency range. The left plot shows ϵ_r' as a function of frequency, and the right plot shows σ for the same materials across the same frequency range.

4.2.3 Graphite Materials

To further explore carbon-based systems, graphite-filled composites were studied at different loadings and using different silicone matrices. Graphite was incorporated into two silicone matrices (C25 and Dragon Skin) at filler loadings of 30 wt% and 45 wt%. As shown in Fig. 4.17, the 45 wt% samples consistently exhibit higher permittivity and conductivity than the corresponding 30 wt% samples for both matrix types.
The choice of matrix also influences the dielectric response, with Dragon Skin-based composites generally showing higher permittivity and conductivity compared to C25-based ones, suggesting differences in filler dispersion or matrix–filler interactions. Despite these improvements, the overall conductivity remains relatively low, with maximum values below approximately 0.8 S/m, which is still far from the target conductivity (7 S/m). Similarly, the permittivity, although significantly increased compared to metal-based systems, does not reach the desired value of approximately 40.

4.2.4 VULCAN Carbon Black Materials

Carbon black-filled composites were investigated as a promising candidate system due to their known ability to form conductive networks at moderate loading levels. VULCAN carbon black[84] was incorporated into the C25 silicone matrix at filler loadings of 15 wt% and 20 wt%. As shown in Fig. 4.18, the composite with 15 wt% carbon black exhibits a relatively high permittivity, approaching the target range ($\epsilon_r \approx 40$), while maintaining moderate conductivity, reaching up to approximately 2.2 S/m at higher frequencies.
However, further increasing the filler loading to 20 wt% results in a significant reduction in both permittivity and conductivity, with values remaining close to those

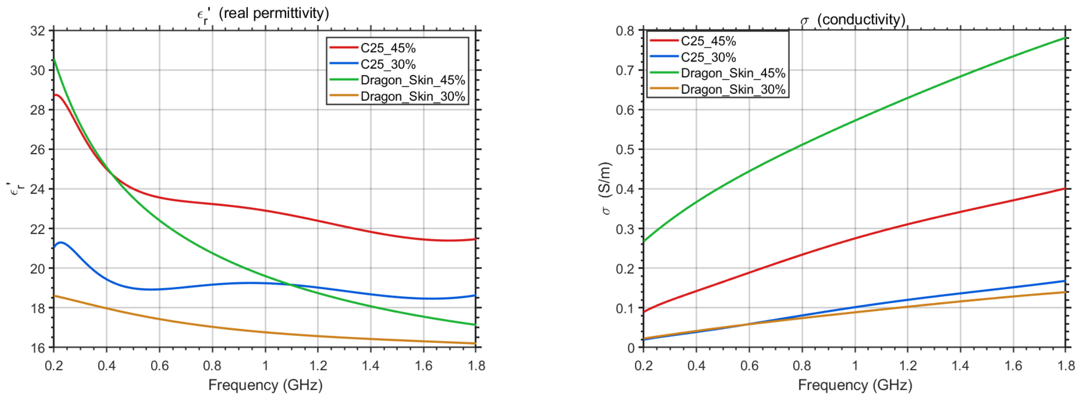

(a) permittivity ϵ_r' **(b)** conductivity σ

Figure 4.17: Real permittivity (ϵ_r') and electrical conductivity (σ) of graphite silicone composites measured over the 0.2–1.8 GHz frequency range. The left plot shows ϵ_r' for four formulations (Dragon Skin 30%, Dragon Skin 45%, C25 30%, and), and the right plot shows the corresponding σ values across the same frequency range.

of the insulating matrix. This unexpected behavior suggests that excessive carbon black content may hinder proper curing or dispersion within the silicone matrix, leading to poor composite formation and the absence of an effective conductive network. Overall, these results indicate that while VULCAN carbon black shows strong potential to achieve the desired dielectric properties at moderate loading, excessive filler content negatively affects the composite structure, preventing further improvement in electromagnetic performance.

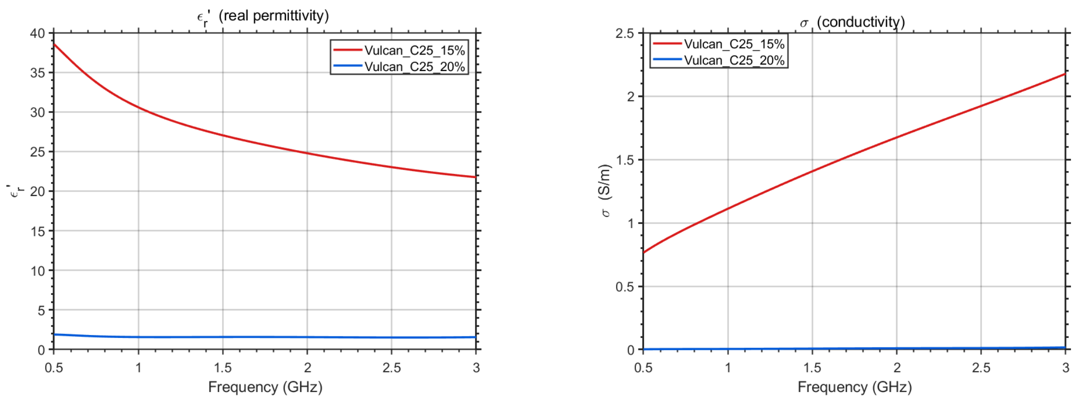

(a) permittivity ϵ_r' **(b)** conductivity σ

Figure 4.18: Real permittivity (ϵ_r') and electrical conductivity (σ) of VULCAN carbon black composites prepared in a C25 silicone matrix, measured over the 0.5–3 GHz frequency range. The left plot shows ϵ_r' for 15 wt% and 20 wt% filler loadings, and the right plot shows the corresponding σ values across the same frequency range.

This subsection also analyzes optimized VULCAN carbon black composites prepared using Ecoflex and food-grade silicone matrices. These systems represent the most promising material candidates among all investigated formulations. Particu-

lar attention is given to the relationship between filler loading, conductivity, and frequency-dependent permittivity.
VULCAN carbon black was incorporated into both Ecoflex silicone and food-grade silicone matrices with varying filler loadings. As shown in Fig. 4.19, both systems exhibit similar overall trends. The electrical conductivity increases significantly with increasing carbon black content, reaching values on the order of 10–20 S/m at 20 wt%, indicating the formation of effective conductive networks near the percolation threshold.
However, the permittivity behavior differs substantially. For the Ecoflex-based system, a pronounced peak in permittivity is observed at low frequencies for the 20 wt% sample, reaching values close to the target ($\epsilon_r \approx 40$), followed by a rapid decrease as frequency increases. In contrast, lower filler loadings show relatively stable but much lower permittivity values. A similar trend is observed for the food-grade silicone system, although the overall permittivity remains lower and more gradual, without reaching the desired target across the measured frequency range.
The Ecoflex and food-grade composites show similar trends in conductivity, with higher filler loadings producing higher σ values across the measured frequency range. In contrast, the permittivity exhibits stronger variation with both filler content and frequency, particularly for the Ecoflex 20 wt% sample, which shows a pronounced decrease in ϵ_r' as frequency increases.
Overall, these results demonstrate that while carbon black composites are capable of achieving high electrical conductivity, maintaining both high and stable permittivity across the frequency range remains challenging. The inherent trade-off between conductive network formation and frequency-dependent polarization limits their ability to fully meet the target dielectric properties.

4.3 Reconstruction Results

The reconstructed images obtained using the DMAS-based method for different target configurations are presented in Fig. 4.20 and Fig. 4.21. These results are used to evaluate the influence of target position and coupling conditions on imaging performance.
Figure 4.20 compares the reconstruction results for the central and lateral target configurations under the same coupling condition. For the central target case (Fig. 4.20(a)), a dominant high-intensity region is observed around $x \approx -20$ mm and $y \approx 40$ mm, which closely matches the true target location. The reconstructed response is relatively compact, although some spatial spreading and low-level artifacts are still visible due to limited aperture and residual noise.
For the lateral target case (Fig. 4.20(b)), the reconstructed target is also correctly localized at approximately $x \approx 40$ mm and $y \approx -20$ mm. However, compared to the central case, the response exhibits increased spatial spreading and pronounced asymmetry, with a clear elongation toward the antenna array. This behavior reflects the impact of asymmetric propagation paths and limited angular coverage, which reduce focusing accuracy.
To further investigate the effect of the coupling medium, Fig. 4.21 presents a direct comparison between the gel-based and air-coupled configurations for the lateral tar-

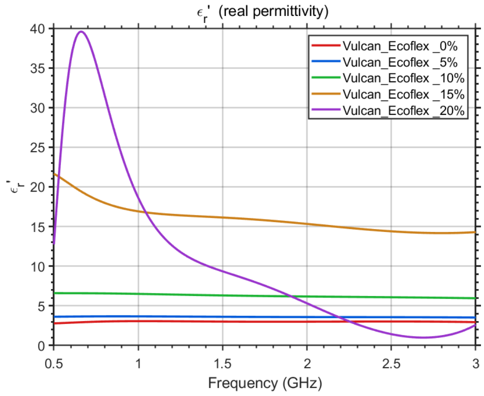

(a) permittivity ϵ_r'

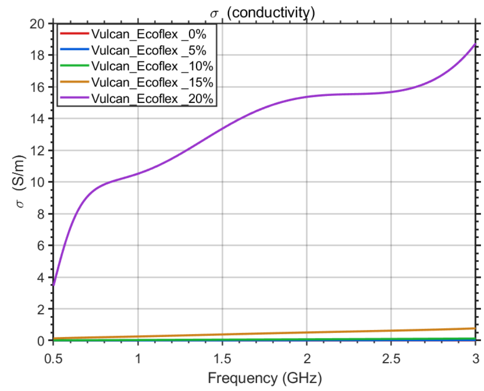

(b) conductivity σ

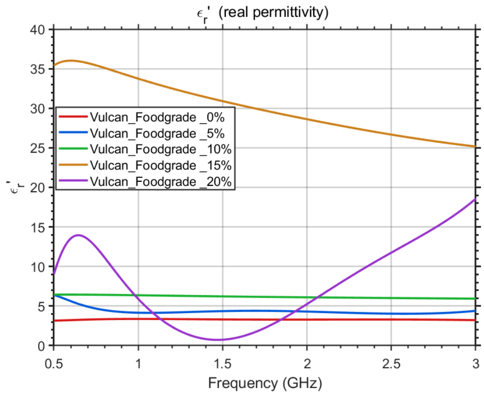

(c) permittivityϵ_r'

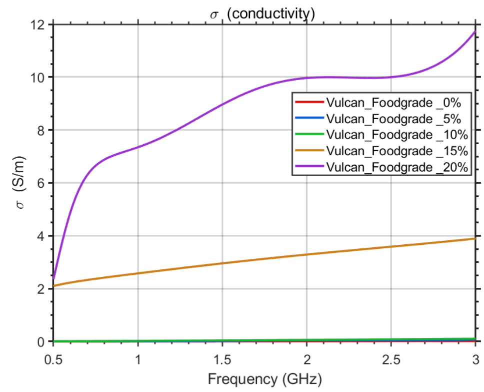

(d) conductivityσ

Figure 4.19: Real permittivity (ϵ_r') and electrical conductivity (σ) of optimized VULCAN carbon black composites prepared using Ecoflex and food-grade silicone matrices, measured over the 0.5–3 GHz frequency range. The top row shows ϵ_r' and σ for Ecoflex-based composites at filler loadings of 0–20 wt%, and the bottom row shows the corresponding ϵ_r' and σ plots for food-grade silicone composites across the same frequency range.

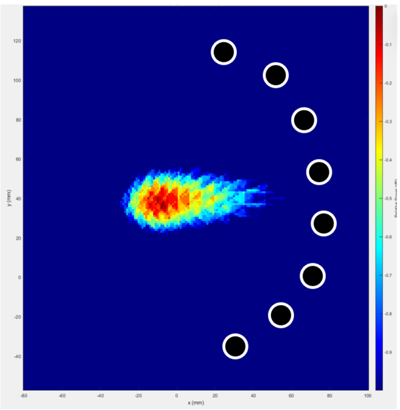

(a) Central target

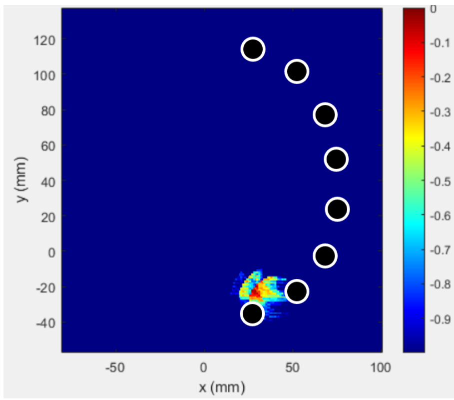

(b) Lateral target

Figure 4.20: Reconstructed images using the DMAS algorithm for different target configurations. (a) Central target case. (b) Lateral target case, showing increased asymmetry and directional artifacts.

get case. In the air-coupled case, the geometry is identical; only the material of the box surrounding the antennas is changed from the coupling gel to air. When the coupling gel is used (Fig. 4.21(a)), the reconstructed target appears more localized, with higher peak intensity and reduced background artifacts. In contrast, the air-coupled case (Fig. 4.21(b)) shows significant degradation, including increased spatial spreading, weaker target intensity, and more pronounced clutter.
The difference between the two cases comes from the coupling efficiency. When the gel surrounds the antennas, its high permittivity allows more energy to enter the phantom, producing stronger signals and a clearer reconstruction. When the surrounding region is set to air, the antennas couple much less efficiently, resulting in weaker fields inside the phantom and a poorer reconstruction. No noise was added to the simulations; the change in image quality is solely due to the difference in coupling medium.
In comparison, the use of a high-permittivity and moderately conductive coupling gel improves impedance matching and facilitates wave penetration into the medium. This reduces boundary reflections and suppresses multipath effects, resulting in improved target localization and image clarity.

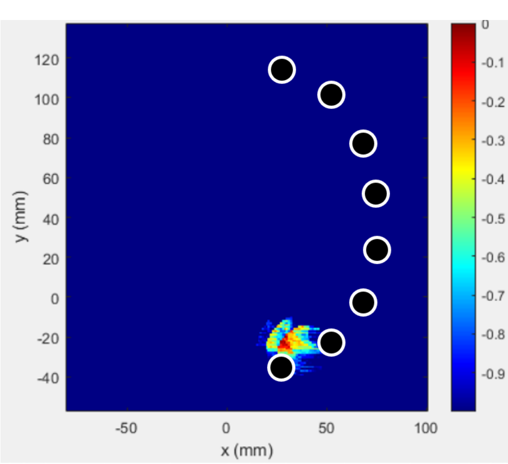

(a) With coupling gel

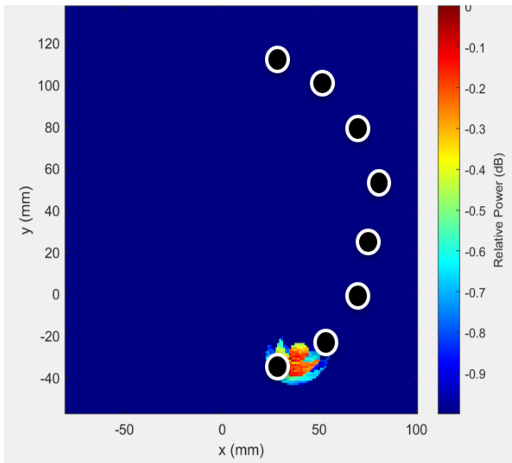

(b) Without coupling gel (air)

Figure 4.21: Comparison of reconstructed images for the lateral target case under different coupling conditions. In both cases, the physical setup is identical; the only difference is the material assigned to the box surrounding the antenna array. (a) With coupling gel, where the surrounding region is filled with the high-permittivity matching medium. (b) Without coupling gel (air), where the same region is assigned air properties.

Overall, these results demonstrate that while the imaging system is capable of detecting targets under both symmetric and asymmetric configurations, the use of an appropriate coupling medium plays a critical role in achieving stable and accurate reconstruction performance.

5
Discussion

5.1 Overview of Key Mechanisms

The behaviour of the microwave imaging system is governed by the interaction between the antenna array, the coupling medium, and the head phantom. The results demonstrate that the dielectric properties of the coupling medium, the geometric configuration of the gel, and the antenna dimensions collectively determine the balance between signal penetration and attenuation. Conductivity controls dissipative losses and lateral wave suppression, permittivity influences resonance behaviour, and geometric parameters shape the near-field distribution and propagation paths. This chapter discusses these mechanisms and interprets their implications for system performance.

5.2 Influence of Coupling Medium Conductivity

Increasing conductivity enhances absorption within the gel, suppressing surface waves and reducing mutual coupling between adjacent antennas. This behaviour is consistent with conductive loss mechanisms described in classical electromagnetic theory, where higher σ increases ohmic dissipation and reduces field penetration depth [71, 68]. The confinement of the electric field near the antenna aperture at high conductivity values further supports this interpretation.
However, the same dissipative mechanism also reduces the energy available for transmission. As conductivity increases, the transmission coefficients decrease substantially, indicating that a significant portion of the radiated energy is converted into heat within the gel. This results in weaker received signals at the other antennas, consistent with the increased volume loss and the rapid field decay observed. Conductivity should therefore be sufficiently high to suppress lateral propagation, but not so high that near-field absorption excessively weakens the transmitted signal.

5.3 Influence of Coupling Medium Permittivity

The permittivity sweep demonstrates that ε_r primarily affects impedance matching and resonance behaviour. Increasing permittivity shifts the resonant frequency downward due to the reduction in guided wavelength, consistent with established antenna theory [71].
Nevertheless, excessively high permittivity introduces detrimental effects. The field

distributions show increased backward radiation and stronger reflections at the gel–phantom interface when ε_r is large. This behaviour can be attributed to the increased impedance contrast between the coupling medium and the phantom, which limits energy transmission into the head. The volume-loss trends further indicate that permittivity influences field confinement rather than intrinsic dissipation, consistent with interfacial polarization phenomena described in dielectric composite literature [100].
Overall, moderate permittivity ($\varepsilon_r \approx 40$) provides the most favourable balance between matching, resonance placement, and forward energy transmission.

5.4 Influence of Gel Geometry

The parametric study of gel dimensions shows that thickness and width play distinct roles. Gel thickness primarily affects the resonant frequency and the propagation path length within the lossy medium. Excessive thickness shifts the resonance outside the desired imaging band and increases attenuation, while insufficient thickness fails to buffer the high-permittivity skin layer. Width, in contrast, influences lateral confinement. Wider gels suppress surface waves more effectively, reducing mutual coupling and multipath interference.
These observations indicate that geometric design must balance attenuation and isolation. Larger gel dimensions improve isolation but degrade signal penetration, whereas smaller dimensions preserve signal strength but allow unwanted lateral propagation. The optimal configuration therefore lies between these extremes, ensuring adequate isolation without compromising the detectable signal.

5.5 Influence of Antenna Dimensions

The antenna length strongly determines the resonance frequency and radiated power. Longer antennas exhibit lower resonant frequencies due to increased electrical length, while shorter antennas resonate at higher frequencies. This behaviour aligns with classical monopole antenna theory [68]. The immersion depth, by contrast, has minimal influence on resonance but affects coupling strength. Shallow immersion reduces the propagation path within the lossy gel, improving transmission, whereas deeper immersion increases attenuation.
The combined effect of antenna length and depth reinforces the importance of tuning the radiating element to the desired frequency band while minimizing unnecessary propagation through lossy media.

5.6 Dielectric Characterization Results

The dielectric characterization of the synthesized carbon-black-loaded silicone composites provides a direct assessment of their suitability as coupling media for microwave head imaging. The measured conductivity and permittivity values show that the electrical response of the composites is strongly governed by the carbon

black content, confirming that the filler network dominates over the silicone host in determining the effective dielectric properties.
A pronounced increase in conductivity is observed as the carbon black loading approaches higher concentrations. This behaviour is characteristic of percolation phenomena, where previously isolated conductive particles begin to form continuous pathways through the insulating matrix [96, 97]. Once these pathways are established, small changes in filler content lead to large changes in bulk conductivity. In the context of the coupling medium, this implies that attenuation can be tuned over a relatively wide range by adjusting the filler fraction, allowing the designer to control the trade-off between penetration depth and lateral wave suppression.
The permittivity measurements exhibit a strong dispersion at lower frequencies, with elevated values that gradually decrease as frequency increases. This trend is consistent with interfacial polarization and microcapacitive effects between neighbouring carbon black particles [100]. At low frequencies, charge carriers have sufficient time to accumulate at particle–matrix interfaces, enhancing polarization and increasing the effective permittivity. As the frequency rises, the carriers can no longer follow the rapid field oscillations, causing the interfacial contribution to diminish and the permittivity to drop. The observed behaviour confirms that the composites act as dispersive media, but within the 0.5–1.5 GHz band of interest, the variation remains sufficiently moderate to ensure predictable coupling performance.
From an application standpoint, the characterized dielectric properties support the use of these CB–silicone composites as practical coupling gels. The achievable conductivity range is high enough to provide meaningful attenuation of surface waves, yet can be limited to avoid excessive loss of penetrating signals. Similarly, the permittivity values at relevant filler loadings are close to those of brain tissue, which reduces impedance mismatch at the gel–phantom interface and improves energy transfer. These findings indicate that the synthesis process yields materials whose dielectric properties can be tailored to meet specific imaging requirements, while maintaining stability and reproducibility across the operating band.

5.7 Implications for Imaging Performance

The imaging results indicate that the coupling gel improves reconstruction quality by suppressing multipath signals and reducing unwanted lateral wave propagation. When the antennas are immersed in the gel, the lossy medium attenuates surface waves that would otherwise travel along the array boundary and interfere with neighbouring channels.
The central target is reconstructed more accurately due to the symmetric propagation paths available in the array geometry. For the lateral target, the reconstruction exhibits increased spatial spreading and directional artefacts, which arise from uneven propagation distances and limited angular coverage. These artefacts are inherent to imaging systems and are primarily governed by array geometry rather than the properties of the coupling medium.
Overall, the results show that the gel enhances imaging performance by controlling wave behaviour around the antenna array. Its finite conductivity suppresses lateral propagation and reduces multipath contributions, leading to more uniform and

interpretable measurements.

5.8 Limitations and Interpretation Constraints

The simulation model incorporates several simplifications that influence the interpretation of results. The head phantom is homogeneous and lacks anatomical layers, which may underestimate reflections and impedance discontinuities present in real tissue. No measurement noise or hardware imperfections are included, potentially overestimating reconstruction clarity. These limitations should be considered when extrapolating the findings to experimental or clinical scenarios.

5.9 Summary

The discussion shows that the performance of the microwave imaging system is influenced by the combined effects of dielectric properties, geometric configuration, and antenna design. Among these factors, the most significant finding is that the synthesized carbon-black composite gel effectively suppresses multipath and lateral surface-wave propagation.

6

Conclusion

This thesis investigated the design and optimization of a microwave antenna array system for intracranial hemorrhage detection, with a particular focus on developing a coupling medium capable of suppressing multipath propagation. A simplified head model and a comprehensive set of parametric simulations were used to evaluate how dielectric properties, gel geometry, and antenna configuration influence signal behaviour within the imaging domain.

The results demonstrate that the synthesized carbon-black composite gel provides an effective mechanism for attenuating lateral surface waves and reducing inter-channel interference. This behaviour arises from its finite conductivity, which enables controlled absorption of boundary-guided waves without excessively degrading forward signal propagation. The identified dielectric range, with conductivity between 5–7 S/m and moderate permittivity, offers a practical balance between isolation and penetration for narrowband imaging systems.

Preliminary material synthesis confirmed that carbon-black-loaded silicone composites can achieve the required loss characteristics. Although the measured permittivity exhibits frequency-dependent variability, the material performs favourably near the intended operating band, suggesting that frequency-selective optimization may be more practical than broadband tuning for this application.

Image reconstruction using DMAS further validated the feasibility of the proposed antenna–gel configuration. Both central and off-centre targets were successfully localized, indicating that the system maintains reliable detection capability under idealized simulation conditions.

Future work should focus on refining the dielectric stability of the coupling material, incorporating alternative fillers to improve permittivity control, and extending validation to multilayer head phantoms and experimental measurements. These steps will support the transition from simulation-based feasibility to practical implementation in clinical imaging systems.

Bibliography

[1] World Health Organization, Regional Office for the Eastern Mediterranean, "Stroke, cerebrovascular accident." [Online]. Available: https://www.emro.who.int/ [Accessed: Nov. 14, 2025].

[2] World Stroke Organization, "World Stroke Organization (WSO)." [Online]. Available: https://www.world-stroke.org/ [Accessed: Nov. 14, 2025].

[3] Institute of Medicine, Committee on Nervous System Disorders in Developing Countries, Board on Global Health, *Neurological, Psychiatric, and Developmental Disorders: Meeting the Challenge in the Developing World*. Washington, DC, USA: National Academies Press, 2001.

[4] W. J. Powers *et al.*, "Guidelines for the early management of patients with acute ischemic stroke: 2019 update to the 2018 guidelines for the early management of acute ischemic stroke," *Stroke*, vol. 50, no. 12, pp. e344–e418, Dec. 2019, doi: 10.1161/STR.0000000000000211.

[5] T. Sanna *et al.*, "Cryptogenic stroke and underlying atrial fibrillation," *N. Engl. J. Med.*, vol. 370, no. 26, pp. 2478–2486, Jun. 2014, doi: 10.1056/NEJMoa1313600.

[6] A. Singh *et al.*, "The utility of ultrasound and computed tomography in the assessment of carotid artery plaque vulnerability: A mini review," *Front. Cardiovasc. Med.*, vol. 9, Art. no. 1023562, 2022, doi: 10.3389/fcvm.2022.1023562.

[7] M. Persson *et al.*, "Microwave-based stroke diagnosis making global prehospital thrombolytic treatment possible," *IEEE Trans. Biomed. Eng.*, vol. 61, no. 11, pp. 2806–2817, Nov. 2014, doi: 10.1109/TBME.2014.2330554.

[8] V. L. Feigin *et al.*, "World Stroke Organization: global stroke fact sheet 2025," *Int. J. Stroke*, vol. 20, no. 2, pp. 132–144, 2025.

[9] K. K. Andersen, T. S. Olsen, S. K. Dehlendorff, and H. K. Kammersgaard, "Hemorrhagic and ischemic strokes compared: stroke severity, mortality, and risk factors," *Stroke*, vol. 40, no. 6, pp. 2068–2072, 2009.

[10] S. Y. Semenov, "Microwave tomography: Review of the progress towards clinical applications," *Philos. Trans. R. Soc. A*, vol. 367, no. 1900, pp. 3021–3042, 2009, doi: 10.1098/rsta.2009.0090.

[11] E. C. Fear, "Microwave imaging of the breast," *Technol. Cancer Res. Treat.*, vol. 4, no. 1, pp. 69–82, 2005, doi: 10.1177/153303460500400110.

[12] S. Gabriel, R. W. Lau, and C. Gabriel, "The dielectric properties of biological tissues: III. Parametric models for the dielectric spectrum of tissues," *Phys. Med. Biol.*, vol. 41, no. 11, pp. 2271–2293, 1996, doi: 10.1088/0031-9155/41/11/003.

[13] L. Guo, A. S. M. Alqadami, and A. Abbosh, "Stroke diagnosis using microwave techniques: Review of systems and algorithms," *IEEE J. Electromagn., RF Microw. Med. Biol.*, vol. 7, no. 2, pp. 122–135, Jun. 2023, doi: 10.1109/JERM.2022.3227724.

[14] A. Fhager, S. Candefjord, M. Elam, and M. Persson, "Microwave diagnostics ahead: Saving time and the lives of trauma and stroke patients," *IEEE Microw. Mag.*, vol. 19, no. 3, pp. 78–90, May 2018, doi: 10.1109/MMM.2018.2801646.

[15] P. M. Meaney and K. D. Paulsen, "Addressing multipath signal corruption in microwave tomography and the influence on system design and algorithm development," *Open Access J. Biomed. Eng. Biosci.*, vol. 1, no. 1, pp. 1–7, 2018.

[16] Y. Fang, K. Bakian-Dogaheh, J. Stang, A. Tabatabaeenejad, and M. Moghaddam, "A versatile and shelf-stable dielectric coupling medium for microwave imaging," *IEEE Trans. Biomed. Eng.*, vol. 69, no. 8, pp. 2701–2711, Aug. 2022.

[17] E. Palaimiene *et al.*, "Electrical percolation and electromagnetic properties of polydimethylsiloxane composites filled with Ag nanoparticles of different sizes," *Polymer Compos.*, vol. 41, no. 11, pp. 4750–4756, 2020.

[18] Y. Slimani *et al.*, "Frequency and dc bias voltage dependent dielectric properties and electrical conductivity of $BaTiO_3$–$SrTiO_3/SiO_2$ nanocomposites," *Ceram. Int.*, vol. 45, no. 8, pp. 11989–12000, 2019.

[19] M. J. Abu *et al.*, "Phase structure, microstructure and broadband dielectric response of Cu nonstoichiometry $CaCu_3Ti_4O_{12}$ ceramic," *J. Alloys Compd.*, vol. 683, pp. 579–589, 2016.

[20] P. M. Meaney, C. J. Fox, S. D. Geimer, and K. D. Paulsen, "Electrical characterization of glycerin: water mixtures: Implications for use as a coupling medium in microwave tomography," *IEEE Trans. Microw. Theory Techn.*, vol. 65, no. 5, pp. 1471–1478, May 2017.

[21] H.-S. Lui and A. Fhager, "On the matching medium for microwave-based medical diagnosis," *Biomed. Phys. Eng. Express*, vol. 4, no. 3, Art. no. 035015, 2018.

[22] H.-S. Lui and A. Fhager, "On the matching medium for microwave stroke diagnosis," *Biomed. Phys. Eng. Express*, vol. 5, no. 4, Art. no. 045020, 2019.

[23] C. A. Balanis, *Advanced Engineering Electromagnetics*, 2nd ed. Hoboken, NJ, USA: Wiley, 2012.

[24] S. You, Y. Zhou, L. Zhu, and Q. Wang, "Recent progress in polymer-based high-*k* nanocomposites for energy storage applications," *Nano Select*, vol. 4, no. 6, pp. 1507–1533, Jun. 2023, doi: 10.1002/nano.202200410.

[25] H. Deng, Y. Wang, Y. Han, X. Yu, J. Duan, Z. Huang, and X. Wang, "Finely-reconciled high dielectric constant and low dielectric loss in ternary polymer/Cr_2C_3/montmorillonite composite films," *Current Appl. Phys.*, vol. 21, pp. 650–658, Apr. 2021, doi: 10.1016/j.cap.2020.12.019.

[26] H.-Y. Yao, Y.-W. Lin, and T.-H. Chang, "Dielectric properties of $BaTiO_3$–epoxy nanocomposites in the microwave regime," *Polymers*, vol. 13, no. 9, pp. 1–12, Apr. 2021, Art. no. 1391, doi: 10.3390/polym13091391.

[27] K. Wilczyński, A. Wróblewska, A. Daniszewska, J. Krupka, M. Mrozowski, and M. Zdrojek, "Modulation of dielectric properties in low-loss polypropylene-

based composites at GHz frequencies: Theory and experiment," *Sci. Rep.*, vol. 12, Art. no. 13104, Aug. 2022, doi: 10.1038/s41598-022-17173-4.

[28] L. Wang, X. Chen, L. Jiang, and H. Zhang, "Low-dielectric-constant and low-dielectric-loss polymer composites for high-frequency electronic packaging: A review," *Front. Mater.*, vol. 8, Art. no. 774843, Nov. 2021, doi: 10.3389/fmats.2021.774843.

[29] "FR-4," *Wikipedia, The Free Encyclopedia.* Accessed: Dec. 7, 2025. [Online]. Available: https://en.wikipedia.org/wiki/FR-4

[30] Rogers Corporation, "RO4350B™ laminates—RO4000® series high frequency circuit materials," datasheet, 2022. Accessed: Dec. 7, 2025. [Online]. Available: https://rogerscorp.com/advanced-electronics-solutions/ro4000-series-laminates/ro4350b-laminates

[31] M. T. Sebastian, R. Ubic, and H. Jantunen, "Low-loss dielectric ceramic materials and their properties," *Int. Mater. Rev.*, vol. 60, no. 7, pp. 392–412, Oct. 2015, doi: 10.1179/1743280415Y.0000000007.

[32] J. Chen, H. Zhou, H. Liu, and Z. Xiao, "A low-loss microwave dielectric ceramic with moderate permittivity and near-zero temperature coefficient of resonant frequency," *Sci. Rep.*, vol. 7, Art. no. 14403, Oct. 2017, doi: 10.1038/s41598-017-14333-9.

[33] C. Fang, R. Xiong, and J. Wang, "Recent advances in polymer-based composites for electromagnetic interference shielding: Design, mechanism and applications," *Nano-Micro Lett.*, vol. 15, Art. no. 150, 2023, doi: 10.1007/s40820-023-01123-4.

[34] Y. Guo, F. Xu, X. Chen, and H. Li, "Carbon nanotube based polymer composites for high-performance electromagnetic interference shielding: A review," *Nanoscale Adv.*, vol. 5, no. 4, pp. 1089–1112, 2023, doi: 10.1039/D2NA00685H.

[35] Q. Zhang, Z. Liu, Y. Tan, and S. Zhou, "Conductive polymer composites for efficient electromagnetic interference shielding: Recent progress and future perspectives," *Polymers*, vol. 16, no. 17, Art. no. 2539, 2024, doi: 10.3390/polym16172539.

[36] B. Belaabed, F. Gamard, J.-M. Giraud, A. Rivière, and J.-F. Gerard, "Polyaniline-doped benzene sulfonic acid/epoxy resin conducting composites," *Polym. J.*, vol. 42, pp. 612–620, 2010, doi: 10.1038/pj.2010.41.

[37] H.-J. Kim, S. Lee, Y. Kang, and Y. Kim, "Dielectric loss engineering in conducting polymer-based microwave absorbers," *Polym. Compos.*, vol. 39, no. 2, pp. 410–419, Feb. 2018, doi: 10.1002/pc.24147.

[38] W. Shao and B. Zhou, "Effect of coupling medium on penetration depth in microwave medical imaging," *Diagnostics*, vol. 12, no. 12, 2022.

[39] A. Moradpour *et al.*, "Development of a solid and flexible matching medium for microwave medical diagnostic systems," *Diagnostics*, vol. 11, no. 3, 2021.

[40] W. Wang *et al.*, "Dielectric properties of carbon black filled rubber composites," *Chem. J. Chinese Universities*, 2018.

[41] C. Baumgartner *et al.*, "IT'IS database for thermal and electromagnetic parameters of biological tissues, version 5.0," IT'IS Foundation, Zurich, Switzerland, Tech. Rep., 2025. [Online]. Available: https://itis.swiss/virtual-population/tissue-properties/database/

[42] R. Pethig, *Dielectric and Electronic Properties of Biological Materials.* Chichester, U.K.: Wiley, 1979.

[43] M. Koutsoupidou, E. Groumpas, I. S. Karanasiou, M. Christopoulou, K. Nikita, and N. Uzunoglu, "The effect of using a dielectric matching medium in focused microwave radiometry: An anatomically detailed head model study," *Med. Biol. Eng. Comput.*, vol. 55, no. 5, pp. 809–816, 2017.

[44] J. Yang and A. Kishk, "The self-grounded Bow-Tie antenna," in *Proc. IEEE AP-S Int. Symp.*, 2011, pp. 1452–1455.

[45] S. Abtahi, "Development of UWB Antenna (0.5–5 GHz) for Stroke Diagnosis," M.S. thesis, Chalmers Univ. Technol., Gothenburg, Sweden, 2011.

[46] A. M. de Oliveira, A. M. de Oliveira Neto, M. B. Perotoni, N. Nurhayati, H. Baudrand, A. de Carvalho Jr., and J. F. Justo, "A Fern Antipodal Vivaldi Antenna for Near-Field Microwave Imaging Medical Applications," *IEEE Trans. Antennas Propag.*, vol. 69, no. 12, pp. 8816–8829, Dec. 2021.

[47] B. J. Mohammed, A. M. Abbosh, D. Ireland, and M. E. Bialkowski, "Compact wideband antenna for microwave imaging of brain," *Prog. Electromagn. Res. C*, vol. 27, pp. 27–39, 2011.

[48] Y. Thakkar, X. Lin, Y. Chen, F. Yang, R. Wu, and X. Zhang, "Wearable monopole antennas for microwave stroke imaging," in *Proc. Eur. Conf. Antennas Propag. (EuCAP)*, 2019, pp. 1–5.

[49] M. Tømmer, K. G. Kjelgård, and T. S. Lande, "Body coupled wideband monopole antenna," in *Proc. Loughborough Antennas Propag. Conf. (LAPC)*, Loughborough, U.K., Nov. 2016, pp. 1–5.

[50] L. G. Orozco, L. Peterson, and A. Fhager, "Microwave antenna system for muscle rupture imaging with a lossy gel to reduce multipath interference," *Sensors*, vol. 22, no. 11, Art. no. 4121, 2022, doi: 10.3390/s22114121.

[51] H. Bahramiabarghouei, E. Porter, A. Santorelli, B. Gosselin, M. Popović, and L. A. Rusch, "Flexible 16-antenna array for microwave breast cancer detection," *IEEE Trans. Biomed. Eng.*, vol. 62, no. 10, pp. 2516–2525, 2015.

[52] H. Trefná and M. Persson, "Antenna array design for brain monitoring," in *Proc. IEEE Antennas Propag. Soc. Int. Symp.*, 2008, pp. 1–4.

[53] L. Nguyen, "Microwave Technology for Detecting Torso Injuries: A Pilot Study on Porcine Models," M.S. thesis, Chalmers Univ. Technol., Gothenburg, Sweden, 2019.

[54] P. M. Meaney *et al.*, "Microwave tomography for clinical imaging: Part I—Experimental results," *IEEE Trans. Microwave Theory Techn.*, vol. 50, no. 1, pp. 123–132, Jan. 2002.

[55] P. M. Meaney, K. D. Paulsen, M. W. Fanning, S. P. Poplack, T. D. Tosteson, D. Li, and N. K. V. Yagnamurthy, *Microwave breast imaging with a non-contacting, monopole antenna array.* IEEE Transactions on Medical Imaging, vol. 19, no. 8, pp. 803–813, 2000.

[56] P. M. Meaney, M. W. Fanning, D. Li, S. P. Poplack, and K. D. Paulsen, "A clinical prototype for active microwave imaging of the breast," *IEEE Trans. Microw. Theory Techn.*, vol. 48, no. 11, pp. 1841–1853, Nov. 2000, doi: 10.1109/22.883861.

[57] A. Vander Vorst, A. Rosen, and Y. Kotsuka, *RF/Microwave Interaction with Biological Tissues*. Hoboken, NJ, USA: Wiley-IEEE Press, 2006.

[58] X. Li and S. C. Hagness, *A Confocal Microwave Imaging Algorithm for Breast Cancer Detection*, IEEE Microwave and Wireless Components Letters, vol. 11, no. 3, pp. 130–132, Mar. 2001.

[59] H. B. Lim, N. T. T. Nhung, E. P. Li, and N. D. Thang, *Confocal Microwave Imaging for Breast Cancer Detection: Delay-Multiply-and-Sum Image Reconstruction Algorithm*, IEEE Transactions on Biomedical Engineering, vol. 55, no. 6, pp. 1697–1705, June 2008.

[60] S. Y. Semenov, R. H. Svenson, A. E. Boulyshev, A. E. Souvorov, V. Y. Borisov, Y. Sizov, and G. P. Tatsis, *Microwave tomography: two-dimensional system for biological imaging*, IEEE Transactions on Biomedical Engineering, vol. 43, no. 9, pp. 869–877, Sep. 1996.

[61] P. M. Meaney, K. D. Paulsen, T. Chang, and M. W. Fanning, *Nonactive antenna compensation for fixed-array microwave imaging—Part II: Imaging results*, IEEE Transactions on Medical Imaging, vol. 18, no. 6, pp. 508–518, June 1999.

[62] S. C. Hagness, A. Taflove, and J. E. Bridges, *Two-dimensional FDTD analysis of a pulsed microwave confocal system for breast cancer detection: Fixed-focus and antenna-array sensors*, IEEE Transactions on Biomedical Engineering, vol. 45, no. 12, pp. 1470–1479, Dec. 1998.

[63] S. C. Hagness, A. Taflove, and J. E. Bridges, *Three-dimensional FDTD analysis of a pulsed microwave confocal system for breast cancer detection: Design of an antenna-array element*, IEEE Transactions on Antennas and Propagation, vol. 47, no. 5, pp. 783–791, May 1999.

[64] J. D. Jackson, *Classical Electrodynamics*, 3rd ed., Wiley, 1999.

[65] E. C. Fear, S. C. Hagness, P. M. Meaney, M. Okoniewski, and M. A. Stuchly, “Enhancing breast tumor detection with near-field imaging,” *IEEE Microwave Magazine*, vol. 3, no. 1, pp. 48–56, 2002.

[66] P. M. Meaney, K. D. Paulsen, and A. Hartov, “Microwave imaging for brain applications,” *International Journal of Biomedical Imaging*, 2013.

[67] L. Guerrero, E. Porter, and M. O’Halloran, “Wearable microwave systems for brain imaging: Design and experimental validation,” *IEEE Trans. Antennas Propag.*, 2020.

[68] C. A. Balanis, *Antenna Theory: Analysis and Design*, 4th ed. Hoboken, NJ, USA: Wiley, 2016.

[69] S. Gabriel, R. W. Lau, and C. Gabriel, “The dielectric properties of biological tissues: I. Literature survey,” *Phys. Med. Biol.*, vol. 41, no. 11, pp. 2231–2249, 1996.

[70] S. Gabriel, R. W. Lau, and C. Gabriel, “The dielectric properties of biological tissues: II. Measurements in the frequency range 10 Hz to 20 GHz,” *Phys. Med. Biol.*, vol. 41, no. 11, pp. 2251–2269, 1996.

[71] D. M. Pozar, *Microwave Engineering*, 4th ed. Hoboken, NJ, USA: Wiley, 2012.

[72] D. J. Griffiths, *Introduction to Electrodynamics*, 3rd ed. Upper Saddle River, NJ, USA: Prentice Hall, 1999.

[73] M. Persson, A. Fhager, H. D. Trefný, S. Snygg, M. Elam, L. Nilsson, and J.-E. Karlsson, "Microwave-based stroke diagnosis making its way into clinical trials," *Europhysics News*, vol. 45, no. 4, pp. 22–25, 2014.

[74] R. Scapaticci, L. Di Donato, I. Catapano, and L. Crocco, "Wavelet-based microwave imaging for breast cancer detection," *IEEE Trans. Antennas Propag.*, vol. 60, no. 7, pp. 3526–3531, 2012.

[75] E. C. Fear, S. C. Hagness, P. M. Meaney, Q. Zhou, and J. M. Sill, "Microwave imaging of the breast," *IEEE Trans. Microw. Theory Techn.*, vol. 50, no. 3, pp. 815–827, 2002.

[76] S. Y. Semenov, J. E. Kellam, P. L. Althausen, M. G. Akhadov, M. Bentsman, A. Boukhny, A. E. Souvorov, Y. E. Sizov, and V. G. Pavlovsky, "Microwave tomography for brain imaging: feasibility assessment for stroke detection," *Int. J. Hyperthermia*, vol. 16, no. 6, pp. 455–466, 2000.

[77] A. Fhager, M. Gustafsson, and M. Persson, "3D gradient-based microwave tomography for medical imaging applications," *IEEE Trans. Biomed. Eng.*, vol. 55, no. 9, pp. 2221–2229, 2008.

[78] T. Weiland, "A discretization method for the solution of Maxwell's equations for six-component fields," AEÜ International Journal of Electronics and Communications, vol. 31, pp. 116–120, 1977.

[79] Dassault Systèmes, "CST Studio Suite," Available: https://www.3ds.com/products-services/simulia/products/cst-studio-suite/

[80] M. Clemens and T. Weiland, "Discrete electromagnetism with the finite integration technique," Progress in Electromagnetics Research, vol. 32, pp. 65–87, 2001.

[81] J.-M. Jin, *The Finite Element Method in Electromagnetics*, 3rd ed., Wiley, 2015.

[82] "FEM Convergence Criteria for Electromagnetic Simulation," Available: https://rfessentials.com

[83] A. Belokrys-Fedotov et al., "Adaptive Mesh Refinement for Electromagnetic Simulation," Numerical Methods in Engineering, 2024.

[84] S. K. Kwon, H. J. Kim, and S. W. Kim, "Microwave absorbing properties of carbon black/silicone rubber blend," *Polymer Engineering & Science*, vol. 42, no. 11, pp. 2165–2171, 2002.

[85] J. J. Bond, X. Li, S. C. Hagness, and B. D. Van Veen, *Microwave imaging via space-time beamforming for breast cancer detection*, IEEE Transactions on Antennas and Propagation, vol. 51, no. 10, pp. 2905–2913, Oct. 2003.

[86] S. A. Shah Karam, D. O'Loughlin, B. L. Oliveira, M. O'Halloran, and B. Mohammadzadeh Asl, "Weighted delay-and-sum beamformer for breast cancer detection using microwave imaging," *Measurement*, vol. 177, pp. 109283, 2021.

[87] B. Li, C. A. Randall, and E. Manias, *Polarization Mechanism Underlying Strongly Enhanced Dielectric Permittivity in Polymer Composites with Conductive Fillers*, Journal of Physical Chemistry C, vol. 126, pp. 7596–7604, 2022.

[88] O. A. Al-Hartomy *et al.*, "Dielectric and microwave properties of siloxane rubber/carbon black nanocomposites," *Int. J. Polymer Sci.*, 2011.

[89] Schmid & Partner Engineering AG (SPEAG), "DAK: Dielectric Assessment Kit Product Brochure," MWF Corporation. [Online]. Available: `https://`

www.mwf.co.jp/assets/pdf/products/speag-dak_ja.pdf [Accessed: June 26, 2026].
[90] Rohde & Schwarz, "R&S®ZNBT Vector Network Analyzer Product Page." [Online]. Available: https://www.rohde-schwarz.com/us/products/test-and-measurement/vnas/rs-znbt-vector-network-analyzer_63493-58917.html [Accessed: June 26, 2026].
[91] Siepel, "SEA-FE Ferrite Absorbers – Product Specifications." [Online]. Available: https://www.siepel.com/ [Accessed: Jun. 27, 2026].
[92] Siepel, "EMC Absorbers – Product Catalog." [Online]. Available: https://www.siepel.com/ [Accessed: Jun. 27, 2026].
[93] HITEK Electronic Materials, "ABS-LFE-SA Microwave Elastomer Absorber – Datasheet." [Online]. Available: https://hitek.co.uk/ [Accessed: Jun. 27, 2026].
[94] Laird Performance Materials, "Eccosorb LS-30 Microwave Absorber – Datasheet." [Online]. Available: https://www.laird.com/ [Accessed: Jun. 27, 2026].
[95] Let's Resin, "Liquid Silicone Mold Making Rubber – Food-Grade Silicone." [Online]. Available: https://www.amazon.se/dp/B0G5ZRJK9Y [Accessed: Jun. 27, 2026].
[96] D. Stauffer and A. Aharony, *Introduction to Percolation Theory*, Taylor & Francis, 1994.
[97] S. Kirkpatrick, "Percolation and Conduction," *Reviews of Modern Physics*, vol. 45, no. 4, pp. 574–588, 1973.
[98] A. Celzard, E. McRae, C. Deleuze, M. Dufort, G. Furdin, and J. F. Marêché, "Electrical conductivity of carbonaceous powders," *Carbon*, vol. 34, no. 4, pp. 335–344, 1996.
[99] Y. Li, X. Zhang, and M. Chen, "Polarization mechanisms in conductive polymer composites," *Journal of Applied Polymer Science*, vol. 139, no. 12, 2022.
[100] R. W. Sillars, "The properties of a dielectric containing semiconducting particles," *Journal of the Institution of Electrical Engineers*, vol. 80, no. 484, pp. 378–394, 1937.

DEPARTMENT OF ELECTRICAL ENGINEERING
CHALMERS UNIVERSITY OF TECHNOLOGY
Gothenburg, Sweden
www.chalmers.se

CHALMERS
UNIVERSITY OF TECHNOLOGY